IEEE Open Journal of
Power Electronics

Received 26 March 2024; revised 30 April 2024; accepted 2 May 2024. Date of publication 8 May 2024;
date of current version 31 May 2024. The review of this article was arranged by Associate Editor Giovanni De Carne.

Digital Object Identifier 10.1109/OJPEL.2024.3398571

Analysis and Dynamic Stabilization of a High-Voltage VSC-MTDC Grid With DC Power Flow Controller Connected to Extremely Weak AC Systems

HASSANIEN RAMADAN A. MOHAMED [1,2] (Graduate Student Member, IEEE), YASSER ABDEL-RADY I. MOHAMED [1] (Fellow, IEEE), AND EHAB F. EL-SAADANY [3] (Fellow, IEEE)

[1]Department of Electrical and Computer Engineering, University of Alberta, Edmonton, AB T6G 1HG, Canada
[2]Departemnt of Electrical Engineering, South Valley University, Qena 83523, Egypt
[3]Advanced Power and Energy Center, Department of Electrical Engineering and Computer Science, Khalifa University, Abu Dhabi 127788, UAE

CORRESPONDING AUTHOR: HASSANIEN RAMADAN A. MOHAMED (e-mail: hrmohame@ualberta.ca)

The work of Hassanien Ramadan A. Mohamed was supported in part by the Ministry of Higher Education of the Arab Republic of Egypt, in part by the Canada First Research Excellence Fund as part of the University of Alberta's Future Energy Systems research initiative, and in part by the Khalifa University of Science and Technology under Grant RC2-2018-006.

ABSTRACT The high-voltage voltage-source converter (VSC)-based multi-terminal dc (MTDC) grid is a key technology for integrating offshore wind energy and enabling bulk power transmission across nations and continents. This paper addresses the small-signal stability of an MTDC grid equipped with a power flow controller (PFC) under extremely weak ac system interconnections. Using a comprehensive linearized state-space model, eigenvalue analysis uncovers that beyond the well-documented low-frequency oscillations (LFO), an MTDC grid may experience unstable medium-frequency oscillations (MFO) under rectifier operation of droop voltage-controlled VSCs when interfaced to an extremely weak ac system. Moreover, it was shown that the most challenging scenario is when multiple droop voltage-controlled VSCs are interfaced to very weak ac systems, with unstable LFO and MFO observed at short-circuit ratio values of 1.4 and 1.8, respectively. Sensitivity analysis is conducted to assess the impact of the droop voltage control gains, PFC control parameters, and dc breaker reactor on the system dominant eigenmodes in such critical weak conditions. Simple yet efficient LFO and MFO compensators are proposed to stabilize the system, and their parameters design was detailed. Extensive simulation studies and real-time validation tests verify the analytical analysis and demonstrate the effectiveness of the proposed compensators and their feasibility for real-time implementation.

INDEX TERMS Critical short-circuit ratio, eigenvalue analysis, multi-terminal dc (MTDC) grid, power flow controller (PFC), sensitivity analysis, small-signal stability.

NOMENCLATURE

A. Variables and Parameters

v_{tdq}	VSC terminal *d-q* axis voltages.
v_{sdq}	PCC *d-q* axis voltages.
v_{gdq}	AC grid *d-q* axis voltages.
i_{gdq}, i_{sdq}	AC grid and VSC *d-q* axis currents.
V_{dc}	DC-link voltage.
P_t	VSC terminal power.
δ	PCC voltage angle.
SC_{MVA}	Short-circuit power at the PCC.
P_{VSC}	VSC rated power.
V_{PFC}	PFC internal voltage.
L_f, C_f, R_f	AC filter inductance, capacitance, and resistance.
L_g, R_g	AC grid inductance and resistance.
C_{dc}	DC-bus capacitance.
G_c	Current loop PI controller.
G_{ac}	PCC voltage PI controller.

G_p	Active power PI controller.
G_{pll}	Synchronization loop PI controller.
k_d	Droop voltage controller gain.
G_{PFC}	PFC current PI controller.
ω_{LF}, k_{LF}	Cut-off frequency and gain of the high-frequency oscillation compensator.
$\omega_{1,2}$, k_{MF}	Cut-off frequencies and gain of the medium-frequency oscillation compensator.

B. Superscripts

c, g	Converter and grid *d-q* reference frames.
$*$	Reference value.
o	Steady-state value.

I. INTRODUCTION

Motivated by the widespread installation of offshore wind power plants, multi-terminal high-voltage dc (MTDC) transmission systems based on the voltage-source converter (VSC) technology have received significant attention from industry and academia. Unlike point-to-point HVDC transmission, MTDC grids offer greater operational flexibility and improved supply reliability and security [1]. Moreover, MTDC grids can be used to interconnect multiple asynchronous ac systems in different countries and continents, allowing the share of diversity in renewable energy resources [2]. Currently, several MTDC grid projects are in the planning phase and are predominantly aimed at facilitating large-scale wind energy transmission. Among these are the envisioned European Super Grid in the North Sea and the Atlantic wind connection project along the United States eastern seaboard [3], [4]. Despite the enormous benefits of MTDC grids, they present distinct challenges, such as protection against dc faults, power flow management, and stability problems due to the dynamic interactions with existing ac systems.

Multiple studies indicated that integrating VSC-HVDC lines can improve power system stability, particularly enhancing small-signal and transient stability [5], [6], [7]. This enhancement results from their capability to independently control active and reactive power, coupled with the incorporation of power oscillations damping features. However, MTDC grids, due to their complex dynamics, are prone to instability, which may stem from dc side resonances, the dynamic interactions between multiple converters, and the interactions with host ac systems. Hence, investigating and addressing the stability problem and dynamic performance of MTDC grids have been reported in numerous studies [8], [9], [10], [11], [12], [13], [14], [15], [16], [17], [18], [19], [20], [21]. Two main methodologies are employed to assess the small-signal stability of an MTDC grid: modal analysis and frequency domain analysis. Modal analysis, which relies on detailed linearized state-space models, helps identify the system's oscillatory modes and key states influencing them. Frequency domain analysis, utilizing impedance models, is advantageous for analyzing highly complex systems where complete knowledge of all system parameters is challenging.

The MTDC grid instabilities stemming from the dc-side resonances have been investigated in [8], [9], [10]. These resonances are caused by poorly damped LC circuits in the dc network, and the likelihood of resonance instability rises with an increase in the number of nodes and branches within the MTDC grid. Furthermore, the resonance frequency becomes more prominent as the line length increases, which constrains the bandwidth of the dc voltage controller [11]. The impact of various droop control structures on the MTDC grid power transfer limits was evaluated in [12]. In [13] and [14], a reduced-order modeling approach is applied to reduce the model complexity and enhance simulation efficiency. The study in [15] evaluates the dc voltage oscillations and stability of an MTDC distribution system using an improved reduced order model based on a dynamic restructuring technique. Reference [16] presents a simplified modular multi-level converter (MMC) model to assess the dynamics and stability of a meshed MTDC network.

Stability analysis and dynamic interactions between MTDC grids and the host ac systems are presented in [17], [18], [19]. The work in [17] showed that interactions between an MTDC grid and ac systems are prominent following converter outages and faults on either ac or dc side, with instability often attributed to the dc-side states. In [18], it was revealed that the droop voltage controlled VSCs as the source of dc voltage oscillations in the MTDC grid. It also demonstrated that power flow reversal may lead to dc voltage oscillations. The impact of dynamic interactions between multiple converters on the MTDC grid stability was presented in [20], [21]. A sensitivity analysis approach was proposed in [20] based on impedance modelling to analyze the stability and dynamic interactions in a multi-vendor MTDC grid. In [21], a comprehensive small-signal model was developed to study the interactions between VSCs in an MTDC grid and explore the influence of VSCs operating points and controller parameters on these interactions. However, the studies mentioned above commonly presume a stiff ac system when evaluating the MTDC grid stability and dynamics. This assumption may not hold, especially when VSCs are connected to very long transmission lines, which can significantly reduce the strength of the ac system.

The stability of a single VSC interfaced with a weak ac system has been widely investigated in the literature. It was reported that low-frequency oscillations may jeopardize the stable operation of a VSC due to the coupling between the conventional phase-locked loop (PLL) and the ac system dynamics [22], [23]. A smaller PLL bandwidth can enhance the VSC stability, though it may compromise the robustness and transient performance of the system [24]. Therefore, advanced PLL designs [23], [25], and alternative synchronization methods such as artificial point of common coupling (PCC)-based synchronization techniques [24] and the power synchronization control (PSC) [26] have been proposed to ensure the stability and robustness of VSCs under weak grids. However, the PSC approach can compromise the converter performance during fault conditions due to the absence of direct current

control, necessitating a switch back to the vector control strategy to limit converter current [27], [28]. Moreover, it can result in instability and sub-synchronous resonance in stiff grids due to voltage conflict, as reported in [29], [30]. Additionally, practical applications of the PSC for regulating HVDC converters on a large scale remain limited [31].

Further research indicated that the VSC instability is not solely linked to the PLL but also due to interactions of various control loops, including outer and inner control loops of the classical vector control, suggesting that enhancement in control strategies, like restructuring controllers or introducing multi-variable controllers, could mitigate the instability challenge [32], [33]. However, these insights may not directly apply to VSCs connected to weak grids within MTDC grids, especially when droop voltage control is implemented, due to the potential of increased interactions among VSCs. The small-signal stability of an MTDC grid interfaced with weak ac systems was investigated in [34], [35], [36]. In [35], a methodology based on participation factor analysis was proposed to distinguish local and inter-area oscillation modes. It was shown that the interactions between VSCs largely depend on the short-circuit ratio (SCR) values and PLL gains. The work in [34] showed that the coupling effect of the VSC outer control loops under a weak grid leads to system instability, the coupling effect that becomes stronger in MTDC systems. Nonetheless, these studies did not examine the MTDC grid stability under extreme conditions, such as when SCR approaches 1, nor did they identify the critical short circuit ratio (CSCR) for VSCs under rectifier and inverter operations. Moreover, the impacts of droop controller gain, PFC control parameters and dc circuit breaker were not assessed.

Apart from dynamic stability, the protection of an MTDC grid against dc faults is a major challenge. The MTDC grids have very low impedances, complicating the fault current interruption process [37]. Hence, dc circuit breakers are proposed in the literature. One key component of these breakers is the dc reactor, which facilitates fault current interruption by limiting its rate of rise. The inductance of these reactors is typically within the range of hundreds of microhenries [38]. The work in [39], [40] evaluated how bringing these inductors into MTDC grids impacts their dynamic stability. It was found that as the MTDC grid inductance increases, resonances become more prominent and are observed at low frequencies, which may lead to system instability. However, the impact of dc breaker reactors when an MTDC grid is connected to weak ac systems was not addressed.

In a meshed MTDC grid, managing power flow across various transmission lines is crucial to avoid overloading and ensure the economic operation of the grid. To this end, DC power flow controllers (PFCs) have been introduced to manage MTDC grids effectively. The PFCs are dc/dc converters that insert a variable voltage into the transmission lines, thus controlling the current flow. They are categorized into series-connected [41], [42] and parallel-connected PFCs [43], [44]. Series-connected PFCs are generally preferred owing to their compact design and cost-effectiveness compared to parallel-connected PFCs. The latter requires the capability to withstand the nominal dc voltage, making them less economical and bulkier. Besides power flow control, PFCs can improve the MTDC grid damping, as demonstrated in [39], [45], [46]. The research in [39] and [46] suggested adding active damping controllers to the PFC control system to reduce MTDC grid voltage and current oscillations stemming from dc-side resonance. It was shown that the PFC-based damping controller is capable of improving the stability margin by shifting the dominant eigenmodes further into the left half plane (LHP). Conversely, [45] aimed to broaden the PFC functionality by including the suppression of power oscillations that occur due to faults on the ac side. A new active compensator was proposed, using a proportional-resonant controller combined with the PFC control setup. While these studies demonstrated the damping enhancement capability of PFC, the literature has yet to fully explore the capability of PFCS in stabilizing an MTDC grid under weak system conditions, presenting an opportunity for further investigation.

Based on the literature survey, the existing studies have not assessed the stability of an MTDC grid when the SCR approaches 1. Further, the influence of PFC control parameters, dc breaker reactor, and droop voltage controller gains in such critical conditions have yet to be examined. Moreover, the potential role of PFC in stabilizing an MTDC grid has not been reported. This paper aims to address these research gaps, with the primary contributions outlined as follows:

1) A comprehensive small-signal stability analysis of an MTDC grid equipped with a PFC interfacing extremely weak ac systems is conducted based on a detailed linearized state-space model. The eigenvalue analysis uncovers that, beyond the well-documented LFOs, an MTDC grid can experience unstable MFO under the rectifier operation of droop-controlled VSCs when connected to very weak ac systems.
2) The CSCR values for the power-controlled and droop voltage-controlled VSCs are identified under both rectifier and inverter operations. Further, the impacts of the PFC control parameters, dc breaker reactor and droop voltage controller gains are evaluated and characterized.
3) Effective stabilization controllers are proposed to mitigate both the LFO and MFO instabilities. Notably, the MFO compensator is integrated with the PFC controller, thereby expanding the PFC functionality to system stabilization in addition to power flow management.
4) Extensive simulation studies and real-time tests are performed to verify the effectiveness of the proposed compensators and their feasibility for real-time implementation.

This paper is organized as follows. The MTDC grid modeling and control is provided in Section II. Section III outlines the MTDC grid stability analysis. The proposed stabilization controllers are presented in Section IV. Section V discusses the simulation studies and real-time tests. Finally, Section VI concludes the paper with a summary of the findings.

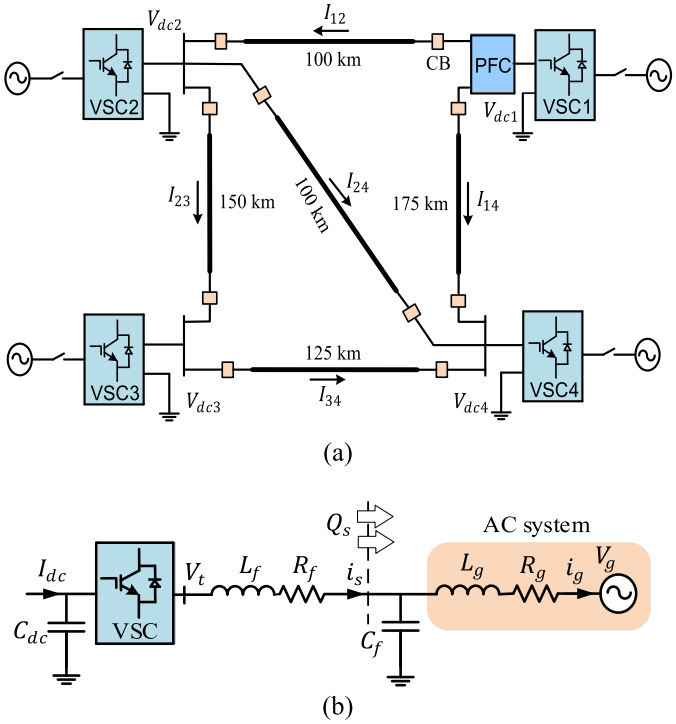

FIGURE 1. (a) MTDC grid schematic diagram (b) VSC ac-side representation.

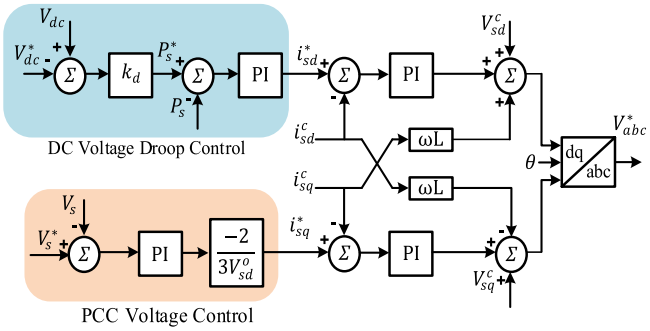

FIGURE 2. VSC control structure.

II. SYSTEM MODELING AND CONTROL

The schematic diagram of the studied typical MTDC grid is illustrated in Fig. 1(a). The practical converter, network and control parameters of the studied MTDC grid are given in the Appendix [51], [52]. The system consists of four VSC stations interfacing the dc network to the ac systems. A detailed representation of the VSC ac-side interface is shown in Fig. 1(b). VSC2 and VSC4 are assumed to carry out the droop voltage control, whereas VSC1 and VSC2 perform active power control, regulating the power injection to the dc grid. The VSCs are connected through a network of five transmission lines on the dc side. A PFC is installed between lines L12 and L14 to regulate their current flow. Circuit breakers are deployed in each line to protect the system in case of dc faults. The following subsections present the modeling of a droop voltage-controlled VSC station, PFC, and dc network. Subsequently, the whole system small-signal model is derived and validated.

A. VSC AC-SIDE MODELING

As shown in Fig. 1(b), each VSC is interfaced with the ac system using an LC filter ($R_f - L_f - C_f$). The strength of the ac system at the PCC is modeled by the grid impedance ($R_g + j\omega L_g$). The ac side dynamics of a VSC in the grid synchronous reference frame (G-SRF) can be described as follows:

$$L_f \frac{di_{sdq}}{dt} = v_{tdq} - v_{sdq} - R_f i_{sdq} - j\omega_g L_f i_{sdq} \tag{1}$$

$$L_g \frac{di_{gdq}}{dt} = v_{sdq} - v_{gdq} - R_g i_{gdq} - j\omega_g L_g i_{gdq} \tag{2}$$

$$C_f \frac{dv_{sdq}}{dt} = i_{sdq} - i_{gdq} - j\omega_g C_f v_{sdq} \tag{3}$$

The SCR is typically applied to characterize the strength of an ac system and is defined as

$$SCR = \frac{SC_{MVA}}{P_{VSC}} = \frac{v_g^2}{Z_g P_{VSC}} \tag{4}$$

B. VSC CONTROL MODELING

The classical vector control structure for a VSC is depicted in Fig. 2. The control strategy includes outer control loops that regulate the dc voltage/active power and the PCC voltage. Additionally, inner control loops are tasked with adjusting the d-q axis output currents of the VSC. To ensure stability and robustness in cascade control, the bandwidth for outer loops generally ranges from 10–20% of that of the inner loops. The outer control loops generate the reference d-q axis currents for the VSC based on

$$i_{sd}^* = \left[-\left(V_{dc}^* - V_{dc}\right) k_d - P_s\right] G_p(s) \tag{5}$$

$$i_{sq}^* = \left(-\left(V_{sd}^* - V_{sd}^c\right) G_{ac}(s)\right) / 1.5 V_{sd}^o \tag{6}$$

The inner current control loops are responsible for producing the reference terminal voltage for the VSC. As depicted in Fig. 2, decoupling terms represented by $j\omega L_f i_{sdq}^c$ are integrated into the current control loops to facilitate independent control of active and reactive powers. Furthermore, PCC voltage feedforward is employed to enhance the VSC robustness under grid voltage disturbances. Based on the inner loop controllers, the d-q axis reference terminal voltages for the VSC can be obtained as

$$v_{td}^* = \left(i_{sd}^* - i_{sd}^c\right) G_c(s) + k_{ff} v_{sd}^c - \omega_g L_f i_{sq}^c - v_{d,AD} \tag{7}$$

$$v_{tq}^* = \left(i_{sq}^* - i_{sq}^c\right) G_c(s) + k_{ff} v_{sq}^c + \omega_g L_f i_{sd}^c - v_{q,AD} \tag{8}$$

In (7) and (8), k_{ff} represents a gain factor which can be adjusted to 1 or 0 to activate or deactivate the PCC voltage feedforward of the current control loops. The terms $v_{d,AD}$ and

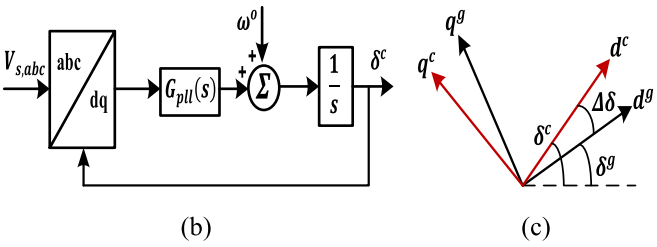

FIGURE 3. (a) PLL control scheme (b) Converter and grid *d-q* frames.

$v_{q,AD}$ are active damping components designed to mitigate the high-frequency oscillations caused by the VSC LC filter resonance [47]. The active damping terms are given by

$$v_{d,AD} = k_{AD}\frac{s}{s+\omega_{AD}}v_{sd}^c \tag{9}$$

$$v_{q,AD} = k_{AD}\frac{s}{s+\omega_{AD}}v_{sq}^c \tag{10}$$

In (9) and (10), the active damping terms are a scaled version of the high-frequency components of the PCC *d-q* voltages, which are added in the counter phase to the current control loops; hence it will be possible to eliminate the oscillations by producing a cancelation effect. A high-pass filter with a cut-off frequency ω_{AD} is utilized to extract the high-frequency oscillations. Meanwhile, the scaling gain k_{AD} adjusts the damping capability of the compensator.

The PLL enables the synchronization of the VSC to the interconnected ac system by extracting the phase angle of the PCC voltage. As depicted in Fig. 3(a), the PLL employs a PI controller ($G_{pll}(s)$) to adjust the angular frequency of the converter *d-q* frame, denoted as ω^c, thereby ensuring v_{sq}^c is set to zero. This angular frequency is subsequently integrated to yield the synchronization angle, δ^c, according to

$$\delta^c = \frac{1}{s}[G_{pll}(s)\, v_{sq}^c + \omega^o] \tag{11}$$

Accurate modeling of the PLL dynamics is critical for evaluating the stability of VSC, especially under weak grid conditions. A key factor for VSC accurate modeling involves the consideration of two distinct *d-q* reference frames: the ac grid and converter frames. As illustrated in Fig. 3(b), these frames align in a steady state; however, transient disturbances lead to a phase shift between them due to the PLL's response time. To accurately model the VSC, it is crucial to uniformly represent all the variables in either the grid's or the converter's *d-q* frame. Based on Fig. 3(b), the two *d-q* frames can be related according to

$$f_{dq}^c = f_{dq}e^{-j\delta^c}e^{j\delta} = f_{dq}e^{j-\Delta\delta} \tag{12}$$

C. PFC MODELING

The PFC topology implemented in this study for managing the transmission line currents I_{12} and I_{14} is depicted in Fig. 4. It consists of an auxiliary dc/dc converter used to regulate

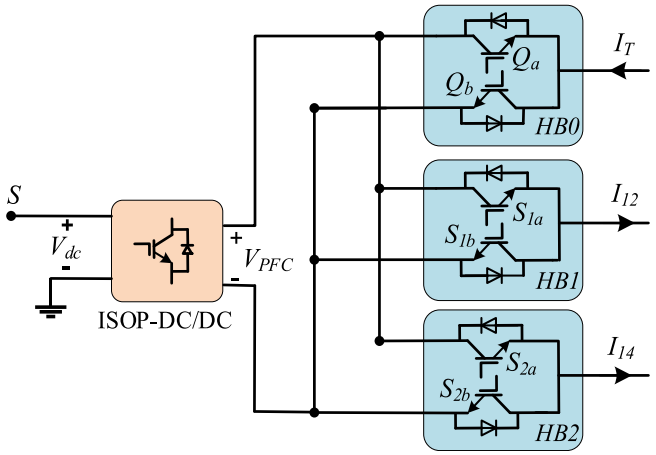

FIGURE 4. PFC topology schematic diagram.

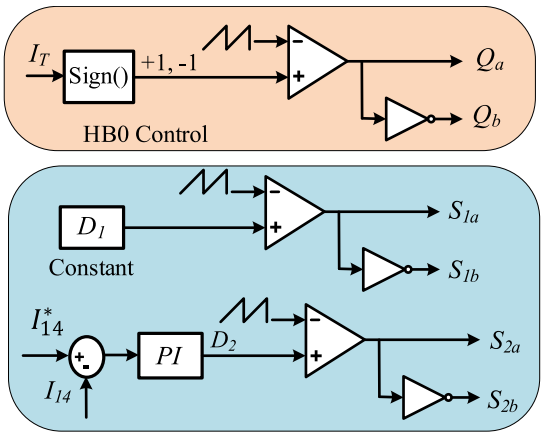

FIGURE 5. PFC control structure.

the PFC internal voltage, denoted as V_{PFC}. Each transmission line is connected to a half-bridge (HB), which introduces a controllable series voltage into the lines, thereby allowing the regulation of the current flow. With the current configuration, as in Fig. 4, the switch Q_b of HB0 will be maintained in the on-state. Meanwhile, turning on switches S_{1a} and S_{2a} results in the PFC inducing a voltage of $V_{L12} = V_{PFC}$ and $V_{L14} = V_{PFC}$ in each line respectively. Conversely, when the switches S_{1a} and S_{2a} are turned off, the induced voltage will be $V_{L12} = 0$ and $V_{L14} = 0$. The mean voltage applied to each transmission line by the PFC can be mathematically expressed as

$$V_{L12} = D_1 V_{PFC}, \qquad V_{L14} = D_2 V_{PFC} \tag{13}$$

where D_1 and D_2 are the duty ratios of switches S_{1a} and S_{2a}, respectively. A detailed discussion of the PFC operation principle under different current confirmations is elaborated in [48].

The control strategy of the PFC is outlined in Fig. 5. Generally, to regulate the current flow across '*n*' transmission lines, it suffices to actively control only '*n*-1' of those lines. Therefore, for the PFC implemented in this study, only I_{12} or

I_{14} needs to be actively regulated. As illustrated in Fig. 5, a PI controller ($G_{PFC}(s)$) is used to regulate I_{14}. The error between the actual current I_{14} and its reference value I_{14}^* is processed through the PI controller to generate the duty ratio D_2 as

$$D_2 = \left(I_{14}^* - I_{14}\right) G_{PFC}(s) \tag{14}$$

As depicted in Fig. 5, the operation of the switches in HB0 is determined by the flow direction of the current I_T. The transmission line L12 may also be designated as a slack line, whereby HB1 is operated at a fixed duty cycle.

D. DC GRID MODELING

The dynamics of the dc grid voltages can be derived by applying the power balance across the dc link capacitors. For instance, the dc link voltage of VSC1 can be mathematically formulated as

$$\frac{1}{2}C_{dc1}sV_{dc1}^2 = V_{dc1}I_{dc1} - P_{e1} \tag{15}$$

where I_{dc1} is the sum of the transmission line currents at the first terminals ($I_{12} + I_{14}$). Considering a lossless VSC, then

$$P_{e1} = P_{t1} = 1.5\left(v_{td1}i_{sd1} + v_{tq1}i_{sq1}\right) \tag{16}$$

Similarly, the differential equations for voltages $V_{dc2} - V_{dc4}$ can be obtained as

$$\frac{1}{2}C_{dc2}sV_{dc2}^2 = V_{dc2}I_{dc2} - 1.5\left(v_{td2}i_{sd2} + v_{tq2}i_{sq2}\right) \tag{17}$$

$$\frac{1}{2}C_{dc3}sV_{dc3}^2 = V_{dc3}I_{dc3} - 1.5\left(v_{td3}i_{sd3} + v_{tq3}i_{sq3}\right) \tag{18}$$

$$\frac{1}{2}C_{dc4}sV_{dc4}^2 = V_{dc4}I_{dc4} - 1.5\left(v_{td4}i_{sd4} + v_{tq4}i_{sq4}\right) \tag{19}$$

The dc transmission lines are modeled using a π-equivalent model, in which the capacitors at both ends are added to the VSC dc link capacitor and the resultant capacitance is denoted C_{dc}. Hence, the differential equations of the transmission line currents can be formulated as

$$L_{12}sI_{12} = V_{dc1} - V_{dc2} + V_{L12} - R_{12}I_{12} \tag{20}$$

$$L_{14}sI_{14} = V_{dc1} - V_{dc4} + V_{L14} - R_{14}I_{14} \tag{21}$$

$$L_{23}sI_{23} = V_{dc2} - V_{dc3} - R_{23}I_{23} \tag{22}$$

$$L_{24}sI_{24} = V_{dc2} - V_{dc4} - R_{24}I_{24} \tag{23}$$

$$L_{24}sI_{24} = V_{dc2} - V_{dc4} - R_{24}I_{24} \tag{24}$$

where V_{L12} and V_{L14} are the voltages inserted by the PFC to transmission lines L12 and L14, respectively.

E. SMAL- SIGNAL MODEL DERIVATION AND VALIDATION

Equations (1)–(12) describe the nonlinear dynamics of a grid-connected VSC. By applying the perturbation theory, the linear state space model of VSC1 can be derived as in (25).

$$\dot{\tilde{X}}_{VSC1} = A_{VSC1}\tilde{X}_{VSC1} + B_{VSC1}\tilde{U}_{VSC1} \tag{25}$$

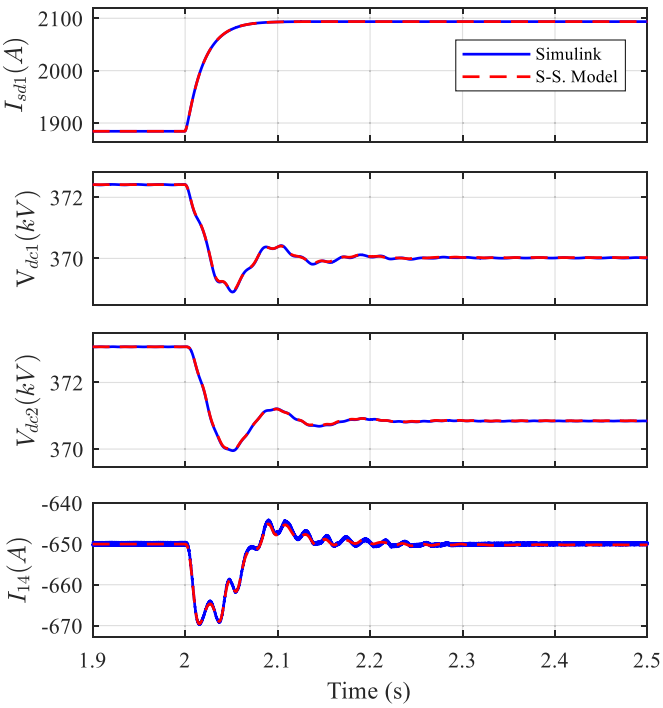

FIGURE 6. Validation of the developed small-signal model.

Similarly, the state-space model of VSC2 −− VSC4 can be obtained. Furthermore, the PFC and dc grid state-space model can be derived by linearizing (13)–(24) as in (26).

$$\dot{\tilde{X}}_{DC} = A_{DC}\tilde{X}_{DC} + B_{DC}\tilde{U}_{DC} \tag{26}$$

Finally, the complete small-signal model of the MTDC grid can be obtained as

$$\dot{\tilde{X}} = A\tilde{X} + B\tilde{U} \tag{27}$$

where $\tilde{X} = [\tilde{X}_{VSC1}\ \tilde{X}_{VSC2}\ \tilde{X}_{VSC3}\ \tilde{X}_{VSC4}\ \tilde{X}_{DC}]^T$ and $\tilde{U} = [\tilde{U}_{VSC1}\ \tilde{U}_{VSC2}\ \tilde{U}_{VSC3}\ \tilde{U}_{VSC4}\ \tilde{U}_{DC}]^T$ are the state and input vectors, respectively. $A = [A_{VSC1}\ A_{VSC2}\ A_{VSC3}\ A_{VSC4}\ A_{DC}]^T$ and $B = [B_{VSC1}\ B_{VSC2}\ B_{VSC3}\ B_{VSC4}\ B_{DC}\ ]^T$ are the characteristics and input matrices, respectively.

The derived small-signal model in (27) is validated against a nonlinear detailed model built in MATLAB/Simulink. As shown in Fig. 6, the system is in a steady state, with the PFC tasked to regulate I_{14} at 500 A. Then, at $t = 2$ s, the power injection of VSC1 is increased by 5%. The close matching between the linearized and nonlinear responses demonstrates the accuracy of the derived small-signal mode.

III. STABILITY ANALYSIS

In this section, eigenvalue analysis is conducted to assess the dynamic stability of the MTDC grid, depicted in Fig. 1, under weak grid conditions. The derived small-signal model in (27) is used to evaluate the influence of SCR variations on the system stability and identify the CSCR for each VSC station under both rectifier and inverter operations. The stability of the MTDC grid is examined across three scenarios of SCR

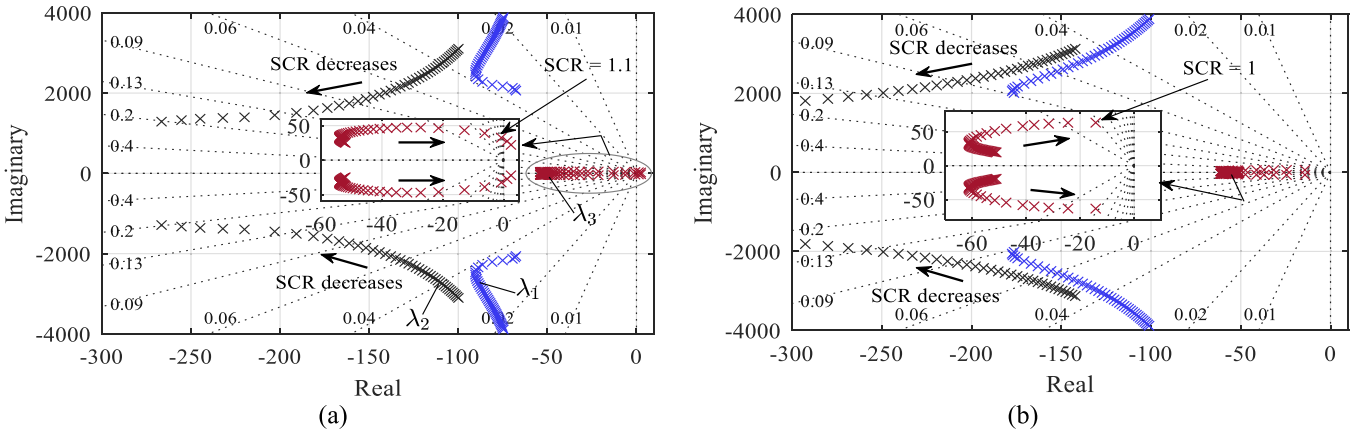

FIGURE 7. Loci of dominant eigenvalues as SCR1 varies from 5 to 1 (a) VSC1 rectifier operation (b) VSC1 inverter operation.

variations: SCR of the power-controlled VSC station (VSC1), SCR of the droop voltage-controlled VSC station (VSC2), and SCR of both droop voltage-controlled VSCs (VSC2 and VSC4). Participation factor analysis (PFA) is conducted to determine the key states that predominantly affect the system's dominant eigenmodes. This analysis facilitates the design of proper stabilization strategies to mitigate potential instabilities and enhance the damping performance of the system. In addition to the eigenvalue analysis, sensitivity analysis is presented to investigate the impact of PFC control parameters, droop voltage controller gain and power loop bandwidth, and DC circuit breaker reactor on the system's stability under weak grid conditions.

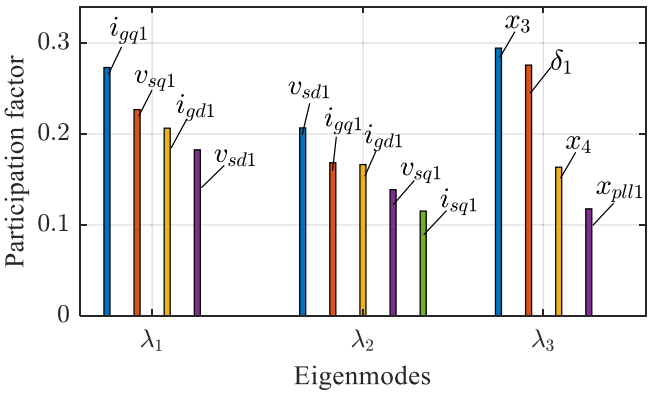

FIGURE 8. Dominant eigenmodes ($\lambda_1 - \lambda_3$) participation factor analysis.

A. MTDC GRID EIGENVALUE ANALYSIS

Fig. 7 illustrates the trajectory of dominant eigenmodes as the SCR of the VSC1 ac system is adjusted from 5 (strong grid) to 1 (extremely weak grid). During rectifier operation, as shown in Fig. 7(a), three eigenmodes, λ_1, λ_2, and λ_3, are notably influenced by SCR variations. λ_1 and λ_2 are high-frequency modes (HFMs), which remain stable across the SCR variations. The PFA reveals that these modes are mainly affected by the ac system states, as detailed in Fig. 8. It should be noted that high-frequency instability has been reported in the literature under weak grid conditions [47]. However, the introduction of the active damping terms ((12) and (13)) in the current control loops effectively mitigates this instability, even under an extremely weak grid, as evident in Fig. 7. Conversely, λ_3, a low-frequency mode (LFM) shifts toward the right-half plane as the SCR decreases and eventually becomes unstable when the SCR reaches 1.1. The PFA in Fig. 8 indicates that λ_3 is predominantly influenced by the outer power loop controller state (x_3), the PLL states (δ_1 and x_{pll1}) and the outer ac voltage controller state (x_4). These findings highlight that low-frequency instability (LFI) emerges under extremely weak grid conditions, primarily due to interactions between the outer control loops and the PLL.

As illustrated in Fig. 7(b), the system's dominant eigenmodes maintain stability across SCR variations in the inverter mode. While the damping of the HFMs improves with higher SCR, the LFM moves toward the right-half plane, indicating reduced damping and potential for poorly damped oscillations. Comparing these findings with those in Fig. 7(a), It can be concluded that the power-controlled VSC station exhibits greater stability margin and robustness during inverter operation than in rectifier mode.

The influence of varying the SCR of the VSC2 ac system from 5 to 1 on the dominant eigenmodes movement is depicted in Fig. 9. It is important to highlight that the HFMs are excluded from the results in Fig. 9 as they maintain stability, and the analysis will primarily focus on the LFMs and medium-frequency modes (MFMs). Under rectifier operation, illustrated in Fig. 9(a), four eigenmodes, λ_4, λ_5, λ_6, and λ_7, are notably impacted by the decrease in the SCR. Specifically, two LFMs (λ_4, λ_5), move closer to the RHP as the SCR decreases, with λ_4 becoming unstable at an SCR of 1.25. According to the PFA presented in Fig. 10, λ_4 is mainly influenced by the controllers' states of VSC2 (encompassing outer loop controllers and PLL) and the dc voltages. Conversely, λ_5, along with the dc voltages, is significantly affected by the controller states of both VSC2 and VSC4, indicating that it is an interaction mode between VSC2 and VSC4. While VSC LFI

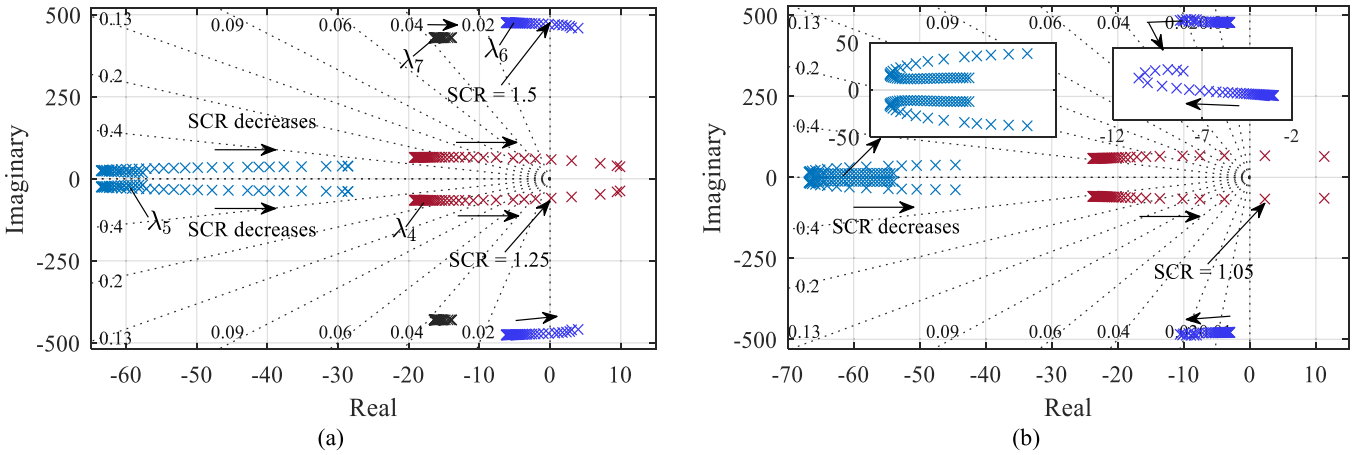

FIGURE 9. Loci of dominant eigenvalues as SCR2 varies from 5 to 1 (a) VSC2 rectifier operation (b) VSC2 inverter operation.

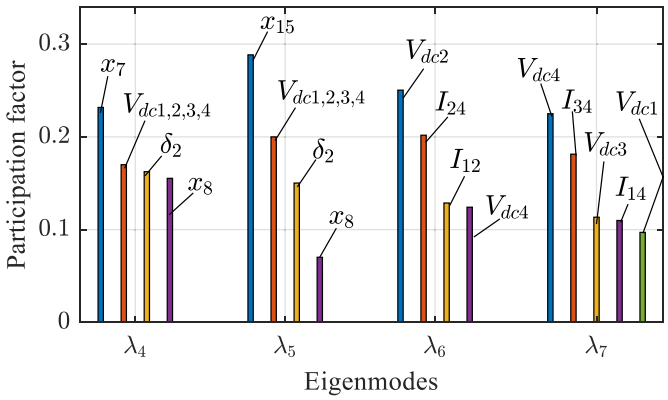

FIGURE 10. Dominant eigenmodes ($\lambda_4 - \lambda_7$) participation factor analysis.

has been reported in the literature under weak grid conditions, Fig. 9(a) reveals that droop voltage-controlled VSCs may also suffer medium-frequency instability (MFI). As demonstrated in Fig. 9(a), λ_6 , an MFM, displays instability at a notably high SCR value of 1.5. Fig. 10 shows that the dc grid states are the main impacting factors on λ_6. It can be concluded that the interaction between the weak ac system and the MTDC grid leads to MFI in droop voltage-controlled VSCs during rectifier operation.

During inverter operation of VSC2, the eigenvalue analysis depicted in Fig. 9(b) indicates that LFI could occur at an SCR value of 1.05, notably lower than the 1.25 threshold in the rectifier mode, highlighting the VSC robustness to weak grid conditions during inverter operation. Contrary to the rectifier operation, the MFM λ_6 initially moves toward the left-half plane as the SCR decreases, indicating improved damping. However, at extremely low SCR values, it slightly shifts toward the RHP without reaching instability, as depicted in Fig. 9(b). Overall, the findings suggest that the operation of a droop voltage-controlled VSC in inverter mode poses fewer challenges under weak grid conditions compared to rectifier mode.

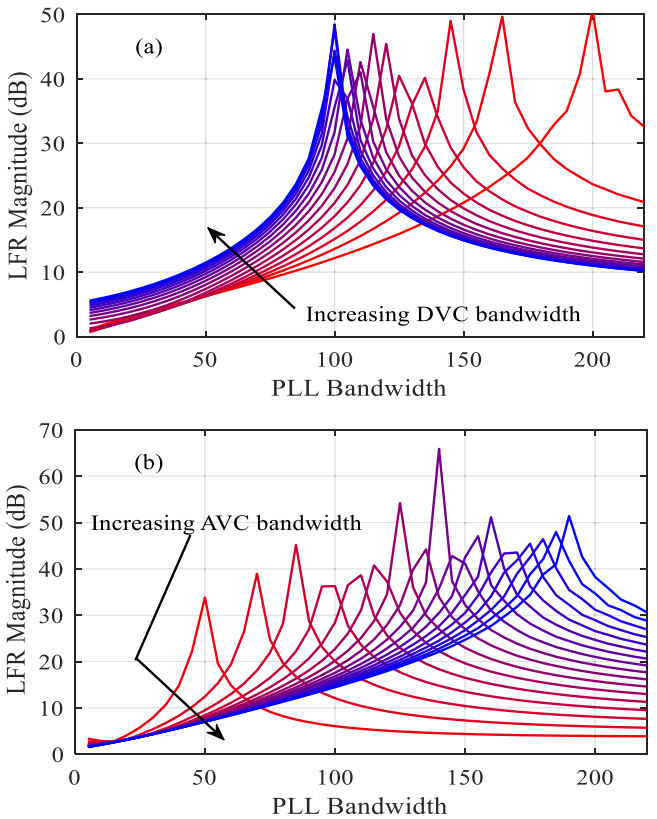

FIGURE 11. LFR magnitude as a function of (a) PLL and DVC bandwidths (b) PLL and AVC bandwidths.

The PFA illustrated in Fig. 10 indicates that the instability of the LFM is primarily driven by dynamic interactions between the VSC outer control loops (droop voltage control (DVC) and AC voltage control (AVC)) and the PLL. To further explore these interactions, Fig. 11(a) shows the low-frequency resonance (LFR) magnitude for varying DVC and PLL bandwidths. This analysis identifies two distinct regions with reduced resonance magnitude at both low and high PLL bandwidths. Specifically, a slower PLL, regardless of the DVC

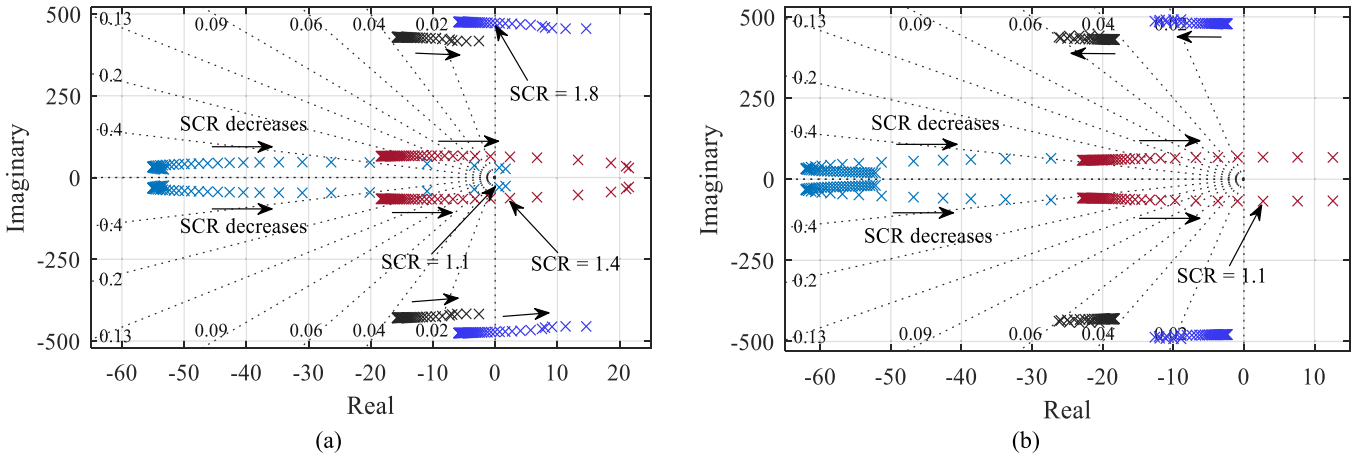

FIGURE 12. Loci of dominant eigenvalues as both SCR2 and SCR4 varies from 5 to 1 (a) Rectifier operation (b) Inverter operation.

bandwidth, significantly reduces the resonance amplitude, indicating lower interactions between the DVC and PLL control loops. Conversely, at higher PLL bandwidths, a slower DVC increases the resonance magnitude, demonstrating increased negative interactions. The most critical condition, characterized by higher resonance amplitude, occurs at mid-range PLL bandwidth and a faster DVC. This case represents the strongest coupling and adverse interactions between the PLL and DVC. Similarly, Fig. 11(b) presents the impact of varying AVC and PLL bandwidths on low-frequency resonance magnitudes. The results indicate that a low PLL bandwidth combined with a fast AVC yields the lowest resonance magnitudes, suggesting minimal interactions between the AVC and PLL. However, increasing the PLL bandwidth alongside a faster AVC leads to higher resonance magnitudes and reduced stability margins. Based on the findings in Fig. 11(b), it is advised to slow down the PLL and increase the AVC bandwidth to mitigate low-frequency resonance.

While the eigenvalue analysis presented in Fig. 7 and 9 examined the effects of varying the SCR for a single VSC on the system stability, the impact of altering the SCR for the two-droop voltage-controlled VSCs is explored. Fig. 12 illustrates the trajectory of the dominant eigenmodes as the SCR for both VSC2 and VSC4 is decreased from 5 to 1. During rectifier operation, the observed eigenmodes movement shows close similarity to the results in Fig. 9(a), where four eigenmodes λ_4, λ_5, λ_6, and λ_7 moves toward the RHP as the SCR decreases. However, the SCR values at which the system becomes unstable are notably different; both λ_4 and λ_6 become unstable at higher SCR values of 1.4 and 1.8, respectively. Furthermore, the LFM λ_5 demonstrates instability at SCR $= 1.1$. In Fig. 13, the PFA indicates that λ_4 is not only affected by the VSC1 controller states but also by those of VSC2, highlighting greater coupling among the droop-controlled VSCs. The findings indicate a greater stability challenge when both droop voltage-controlled VSCs are interfaced with a weak grid. In inverter operation, a parallel trend is observed, as shown in Fig. 9(b), where the MFM shifts

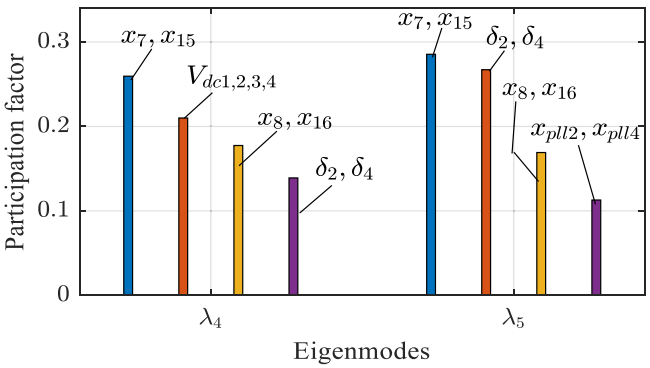

FIGURE 13. Dominant eigenmodes (λ_4 and λ_5) PFA for very weak SCR2 and SCR4.

TABLE 1. CSCR Values of MTDC Grid

VSC connected to weak system	LFO		MFO	
	Rectifier	Inverter	Rectifier	Inverter
VSC1	1.1	--	--	--
VSC2	1.25	1.05	1.5	--
VSC2 and VSC4	1.4	1.1	1.8	--

towards the LHP with decreasing SCR. Conversely, the LFM moves closer to the RHP, reaching instability at an SCR of 1.1.

Table 1 compares the CSCR values for the three eigenvalue analysis scenarios illustrated in Fig. 7, 9, and 12. It is evident that the most critical case that largely challenges the stability of the MTDC system occurs when both droop voltage-controlled VSCs are connected to weak grids.

Based on the eigenvalue analysis presented in Figs 7, 9 and 12, it can be concluded that the dynamic stability of a VSC under extremely weak grid conditions varies depending on whether a VSC performs active power control or droop voltage control. The analysis shows that droop voltage-controlled

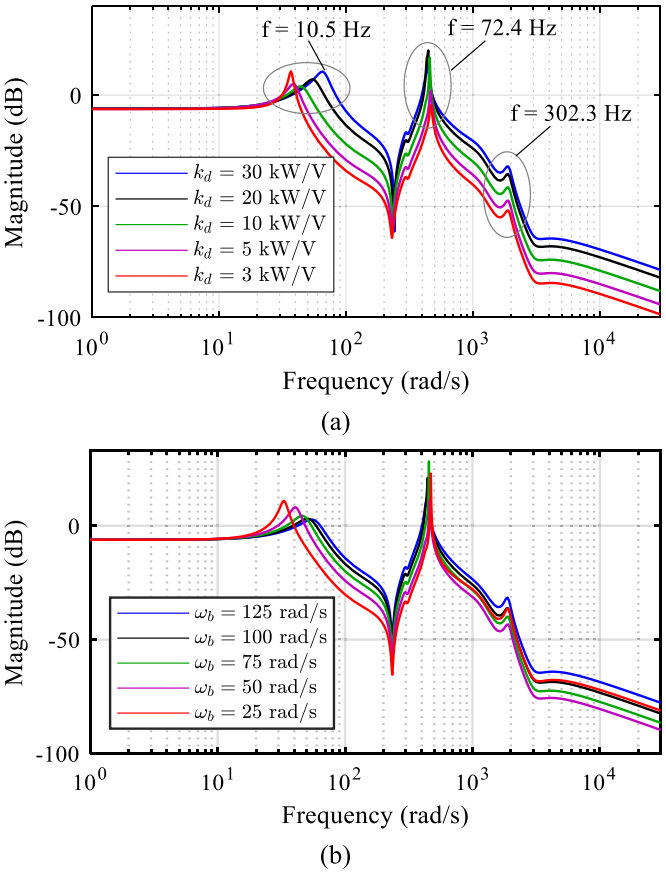

FIGURE 14. Impact of droop voltage controller parameters on the transfer function V_{dc2}/V^*_{dc2} (a) droop gain k_d (b) bandwidth ω_b.

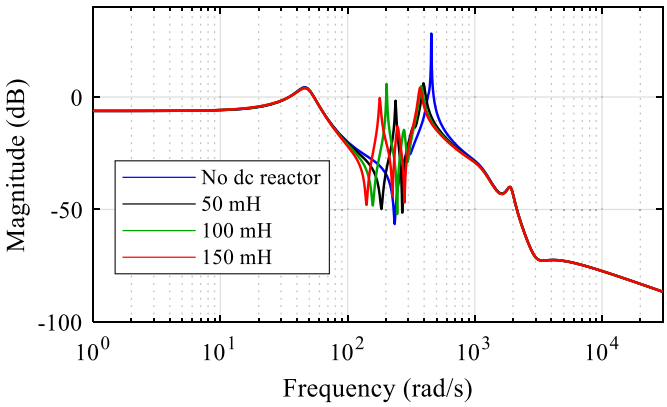

FIGURE 15. Impact of DC breaker reactor on transfer function V_{dc2}/V^*_{dc2}.

VSCs are more prone to instability in weak grid scenarios than power-controlled VSCs. As presented in Table 1, VSC1 only exhibits low-frequency instability at an SCR value of 1 in rectifier operation, while VSC2 may experience both low-frequency and medium-frequency instabilities at higher SCR values of 1.25 and 1.5, respectively. Moreover, increased dynamic interactions between droop-voltage controlled VSCs under weak grid conditions pose significant challenges to the stable operation of an MTDC grid. Notably, when both VSC2 and VSC4 are interfaced to a weak grid, low- and medium-frequency instabilities were observed at SCR values of 1.4 and 1.8, respectively. Based on these findings, it is advised that the strength of the ac grid should be a critical consideration when selecting which VSC stations to perform droop voltage control.

B. SENSITIVITY ANALYSIS

The objective of the analysis in this subsection is to investigate the impact of the MTDC grid critical parameters on the system stability under very weak grid conditions. The frequency response analysis, presented in Fig. 14 and 15, is conducted under rectifier operation of VSC2 at an SCR of 1.15. Fig. 14(a) shows the frequency response of the closed-loop transfer function V_{dc2}/V^*_{dc2} under the variation of the droop voltage controller gain k_d. Three distinct resonance frequencies are identified: LF, MF, and HF resonances, confirming the eigenvalue analysis presented in Fig. 9. As shown in Fig. 14(a), while the variation of k_d has a marginal influence on the HF resonance, its impact on the LF and MF resonance is more pronounced. As the droop gain decreases, the MF resonance amplitude is notably reduced, implying improved damping with little impact on the resonance frequency. On the other hand, the LF resonance amplitude initially decreases as k_d is reduced, but it increases when k_d is higher than 10 kW/V. Moreover, the LF resonance shifts to a lower frequency as k_d decreases. These findings indicate the significant impact of the droop voltage controller gain on the system resonance, highlighting the necessity for precise tuning of k_d to ensure system stability, particularly under weak grid conditions.

The power controller bandwidth is a key parameter besides the droop gain in the VSC outer control loop. Fig. 14(b) illustrates the impact of varying the power control loop bandwidth on the transfer function V_{dc2}/V^*_{dc2}. As Fig. 14(b) reveals, varying the bandwidth (ω_b) has minimal impact on the MF and HF resonances but significantly influences the amplitude and frequency of the LF resonance. Specifically, reducing the power controller bandwidth leads to a higher amplitude of the LF resonance at a lower frequency. This observation indicates that a faster power loop controller would be advisable for stabilizing droop voltage-controlled VSCs connected to weak grids.

The dc reactors are essential components of dc circuit breakers (DCCB) and are needed to control the rate of rise of fault current. Their impact on the system resonance under weak grid conditions considering three different inductance settings is depicted in Fig. 15. The analysis reveals that while the DCCB reactors do not affect the LF and HF resonances, they substantially impact the MF resonance characteristics. A higher DCCB inductance decreases the MF resonance amplitude and frequency. However, it also results in the emergence of another resonance at a lower frequency, which could negatively affect the stability and damping properties of the MTDC grid.

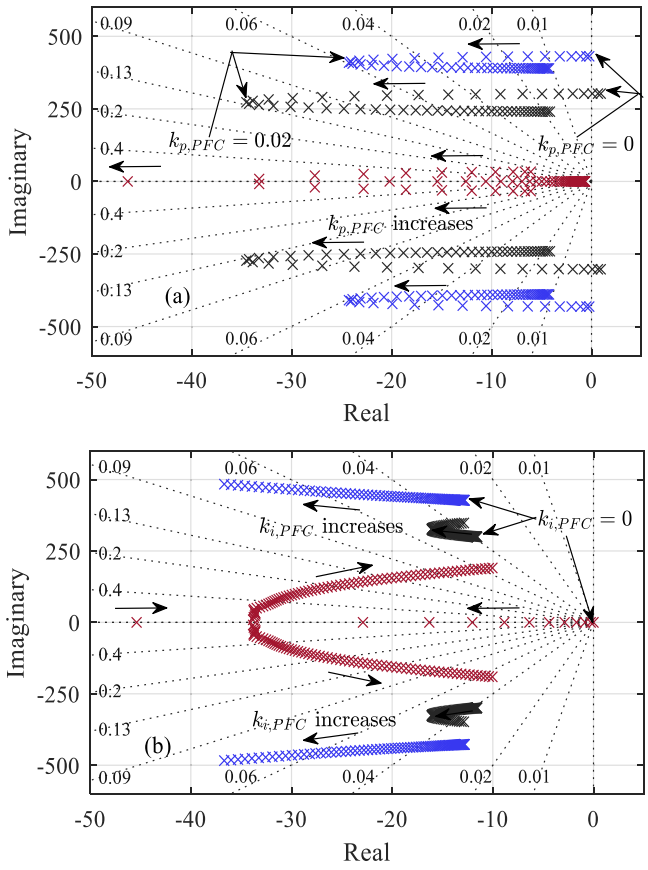

FIGURE 16. Impact of PFC control parameters on dominant eigenmodes under weak grid condition (a) $k_{p,PFC}$ variation (b) $k_{i,PFC}$ variation.

The impact of the PFC control parameters, $k_{p,PFC}$ and $k_{i,PFC}$, on the system eigenmodes is shown in Fig. 16. Fig. 16(a) illustrates the scenario where $k_{i,PFC}$ remains constant at 0.127, while $k_{p,PFC}$ varies between 0 and 0.2. Initially, an increase in $k_{p,PFC}$ enhances the damping of the eigenmodes by shifting them towards the LHP. However, when $k_{p,PFC}$ exceeds 0.02, the eigenmodes transition toward the RHP, indicating a decrease in damping and stability margin. This observation indicates the critical impact of the PFC controller proportional gain under weak grid conditions, as it can significantly influence the system stability margin. In Fig. 16(b), the analysis is conducted with a constant $k_{p,PFC}$ of 0.01, while $k_{i,PFC}$ is adjusted from 0 to 6.5. The eigenmodes movement exhibits similar behavior to that observed in Fig. 16(a), with the modes initially shifting toward the LHP as $k_{i,PFC}$ increases up to 0.306. Beyond this point, although the damping of λ_7 improves, eigenmodes λ_8 and λ_9 migrate toward the RHP. Hence, $k_{i,PFC}$ can be selected to be around 0.306 for the highest stability margin improvement.

IV. STABILITY ENHANCEMENT

As demonstrated in Section III, low-frequency oscillations (LFO) and medium-frequency oscillations (MFO) may compromise the MTDC grid stability when a droop voltage-controlled VSC is interfaced to a very weak grid. These

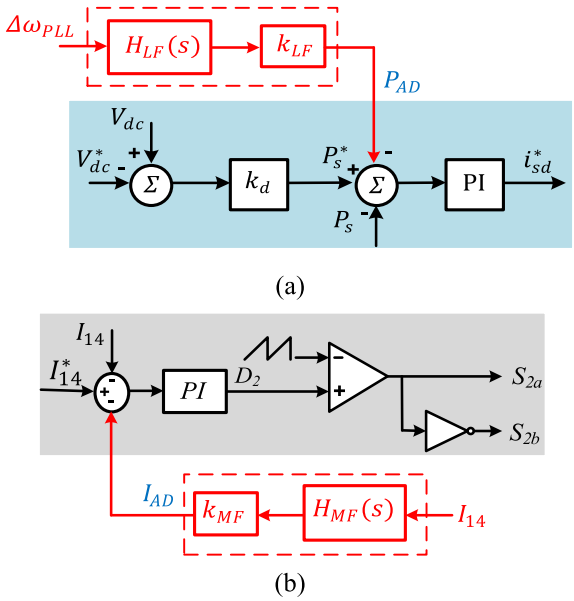

FIGURE 17. (a) LFO compensator integrated with the VSC droop voltage control (b) MFO compensator integrated with the PFC current control.

oscillations become more challenging when multiple droop voltage-controlled VSCs are connected to a very weak grid. To stabilize the system, either passive or active damping techniques can be applied. Passive strategies enhance the system stability margin by incorporating passive elements. Nevertheless, the increased power losses and costs associated with passive damping limit their use in high-power systems. Conversely, active strategies, depicted in Fig. 17, are based on reshaping the system transfer functions by modifying the VSC and/or the PFC control structure to stabilize the system. These methods are widely utilized due to their simplicity and effectiveness.

The general design methodology of the active compensators proposed in this study can be explained using the flowchart shown in Fig. 18. Initially, the unstable eigenmodes and the main states impacting their dynamics are identified using eigenvalue and participation factor analyses, respectively. Based on the PFA, active compensators are developed to insert a damping signal into the control structure of the VSC/PFC. The compensators use a filter (low-, high-, or band-pass filter) to extract the oscillations of the unstable modes, which are then added in a counter phase to specific control loops, producing a cancelation effect. Two design parameters are to be determined for each compensator: cut-off frequency, selected depending on the frequency of the unstable mode, and the compensator gain, fine-tuned to ensure system stability with adequate stability margin.

A. LOW-FREQUENCY OSCILLATION (LFO) COMPENSATOR

The PLL and outer loop controller states are the key states impacting the low-frequency modes, as evidenced by the PFA shown in Fig. 10. Decreasing the bandwidth of the PLL could alleviate the LFO. Yet, it might compromise the system's

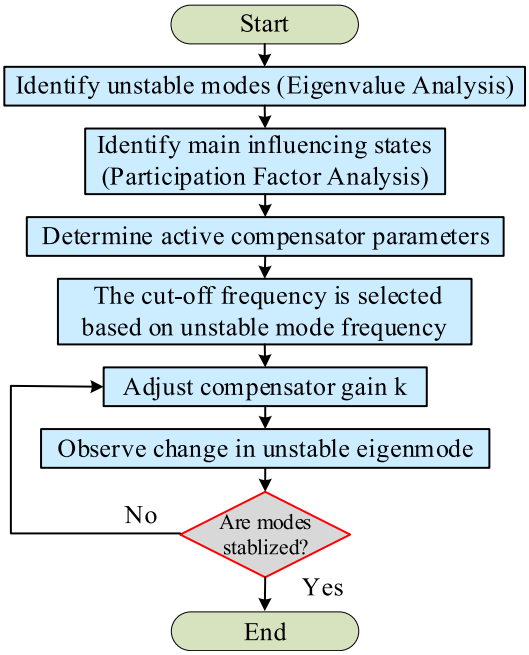

FIGURE 18. Design methodology of proposed compensators.

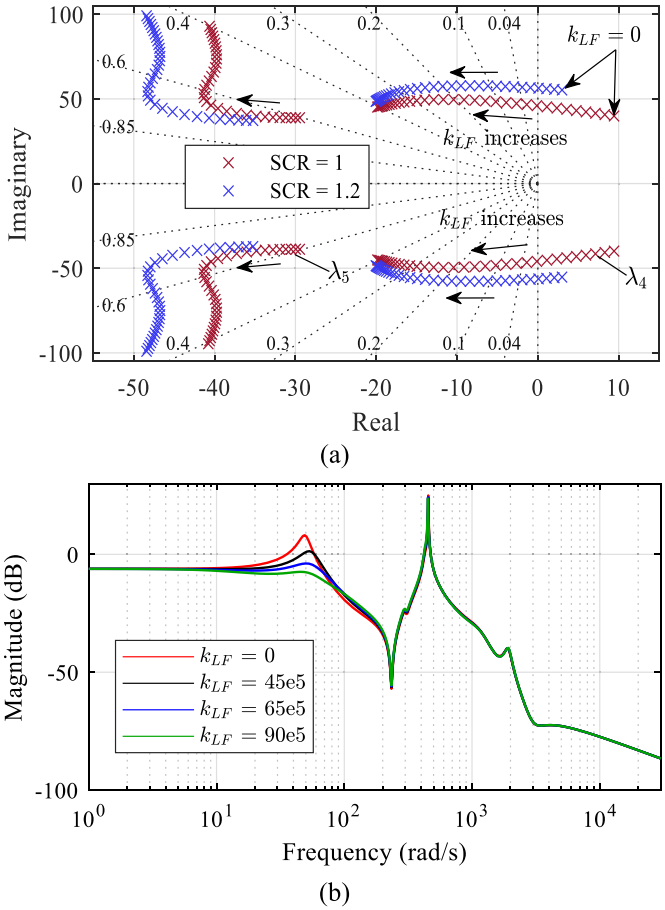

FIGURE 19. Impact of varying the LFO compensator gain on (a) unstable LFMs (b) Transfer function V_{dc2}/V^*_{dc2}.

transient dynamic performance and resilience. Hence, this paper proposes an LFO compensator that integrates a damping signal (P_{AD}) into the VSC outer power loop, as depicted in Fig. 17(a). This active damping signal, a modified version of the PLL output angular frequency ($\Delta\omega_{PLL}$), is introduced in a counter phase to eliminate the LFO by producing a cancelation effect. The LFO compensator output is given by:

$$P_{AD} = k_{LF} \underbrace{\frac{\omega_{LF}}{s + \omega_{LF}}}_{H_{LF}(s)} \Delta\omega_{PLL} \tag{28}$$

In (28), k_{LF} represents the compensator gain factor critical for adjusting the damping efficacy of the compensator. Meanwhile, ω_{LF} signifies the compensator's low-pass filter cut-off frequency. The input of the LFO compensator, $\Delta\omega_{PLL}$, represents the PLL output frequency and the compensator low-pass filter is utilized to prevent the injection of high-frequency oscillations into the VSC outer power loop. The Eigenvalue analysis detailed in Section II has shown that the frequency of the LFMs is approximately 50 rad/s. Thus, a cut-off frequency (ω_{LF}) of 100 rad/s is chosen for the filter. To integrate the dynamics of the LFO compensator included into the system's state space model (27), an additional state is added based on (28).

Fig. 19(a) illustrates the LFMs trajectories as the compensator gain increases from 0 to 120e5 under two settings of SCR values (SCR = 1 and SCR = 1.2). The results clearly demonstrate the ability of the LFO compensator to effectively stabilize the system and remarkably improve the damping of the LFMs. As k_{LF} increases, the unstable mode (λ_4) is shifted toward the LHP, implying improved stability. At very high k_{LF} values (>75e5), the damping enhancement of λ_4 is limited, and the increase in k_{LF} can lead to reduced damping of λ_5 due to a notable increase in its imaginary component. Therefore, a gain of 65e5 can be selected to stabilize the system and ensure an adequate stability margin. At this gain value, the damping ratios of λ_4 and λ_5 are 0.355 and 0.453, respectively.

To further demonstrate the effectiveness of the LFO compensator, the frequency response of the transfer function V_{dc2}/V^*_{dc2} under different compensator gains is depicted in Fig. 19(b). It is evident that as the gain increases, the low-frequency resonance peak is effectively reduced, which is completely mitigated at $k_{LF} = 65e5$. Fig. 19(b) also shows that the LFO compensator specifically targets the low-frequency resonance without affecting the medium- or high-frequency resonances.

B. MEDIUM-FREQUENCY OSCILLATION (MFO) COMPENSATOR

As demonstrated in Fig. 10, the unstable medium-frequency mode (λ_4) is mainly impacted by the dc network states. As the PFC can regulate the line currents and influence their dynamics, this study introduces an MFO compensator integrated into the control scheme of the PFC. As shown in Fig. 17(b),

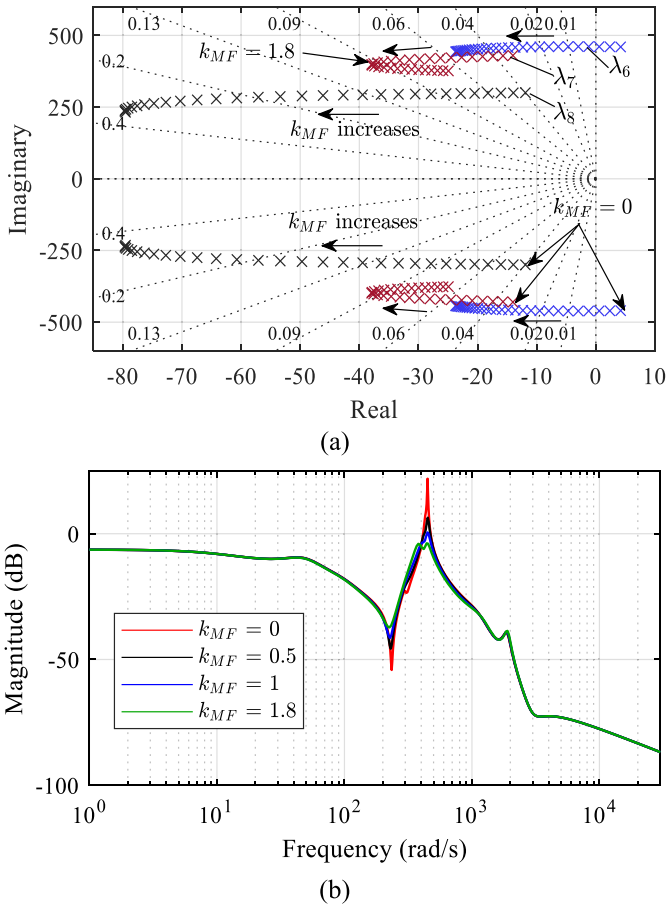

FIGURE 20. Impact of varying the MFO compensator gain on (a) unstable eigenmode (b) Transfer function V_{dc2}/V^*_{dc2}.

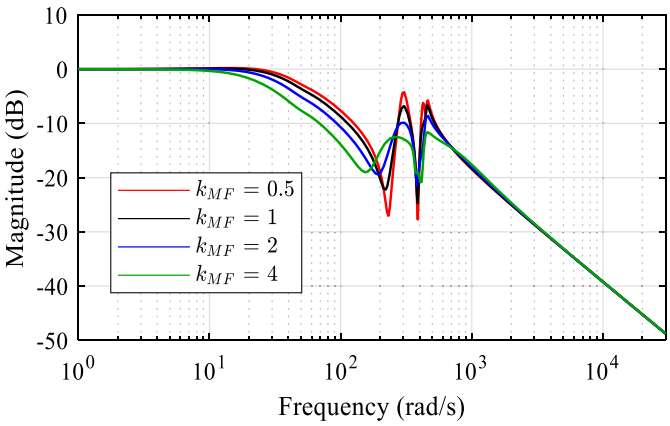

FIGURE 21. Impact of the MFO compensator on the PFC current controller bandwidth.

the MFO compensator employs a band-pass filter to extract the line currents MFO, which is then added to the PFC current control loop in a counter phase. Hence, mitigating the oscillations and stabilizing the system will be possible. The damping signal generated by the MFO compensator can be described by:

$$I_{AD} = k_{MF} \underbrace{\frac{\omega_1}{s+\omega_1}\frac{s}{s+\omega_2}}_{H_{MF}(s)} I_{14} \tag{29}$$

In (29), the band-pass filter is constructed by cascading a low-pass filter (cut-off frequency ω_1) and a high-pass filter (cut-off frequency ω_2). k_{MF} is the MFO compensator gain, which adjusts the compenstor damping effiacy. The center frequency of the band-pass filter is $\omega_0 = \sqrt{\omega_1 * \omega_2}$, determined based on the frequency of the unstable modes. For the band-pass filter in (29), ω_1 is the high cut-off frequency, while ω_2 is the low cut-off frequency of the filter. As indicated in Fig. 9(a), given that unstable MFM has a frequency of 450 rad/s, ω_0 can be set to 450 rad/s. To integarete the MFO compensator dynamics into the system's state space model (27), two additional states are added based on (29).

The influence of increasing the MFO compensator gain from 0 to 3 on the dominant eigenmodes is illustrated in Fig. 20(a). As the compensator gain increases, the unstable eigenmode (λ_6) is relocated to the LHP, thereby restoring the system's stability. Moreover, the eigenmodes (λ_7 and λ_8) are shifted further into the LHP, indicating enhanced damping. However, for k_{MF} values higher than 1.8, the damping of λ_7 is reduced, while the damping improvement of λ_6 becomes minimal. Consequently, a compensator gain of 1.8 can be selected for optimal damping improvement of λ_6 and λ_7 . Fig. 20(b) illustrates the frequency response of the transfer function V_{dc2}/V^*_{dc2} under different gain values with SCR = 1. The results clearly demonstrate the ability of the compensator to effectively mitigate the medium-frequency resonance without impacting resonances at low and high frequencies. It is important to highlight that the result in Fig. 20(b) is obtained with both LFO and MFO compensators implemented. Hence, no low-frequency resonance is observed.

It is essential to evaluate the dynamic interaction between the MFO compensator and the PFC current controller to ensure that the compensator does not compromise the current tracking functionality of the PFC. Fig. 21 illustrates the impact of varying the MFO compensator gain on the PFC closed-loop current controller transfer function (I_{14}/I^*_{14}). While a higher gain value enhances resonance mitigation, it notably reduces the bandwidth of the PFC current controller. For instance, with a gain value of 4, the bandwidth is decreased to 22.4 rad/s compared to 60 rad/s in the absence of the compensator. Hence, the design of the compensator gains should consider not only the stability enhancement but also the impact on the PFC's current tracking capability.

V. VALIDATION RESULTS

Extensive time-domain simulation tests are performed to validate the analytical analysis presented in Sections III and to verify the efficacy of the proposed LFO and MFO compensators in Section IV. A detailed nonlinear model of the MTDC grid, depicted in Fig. 1, was developed in MATLAB/Simulink

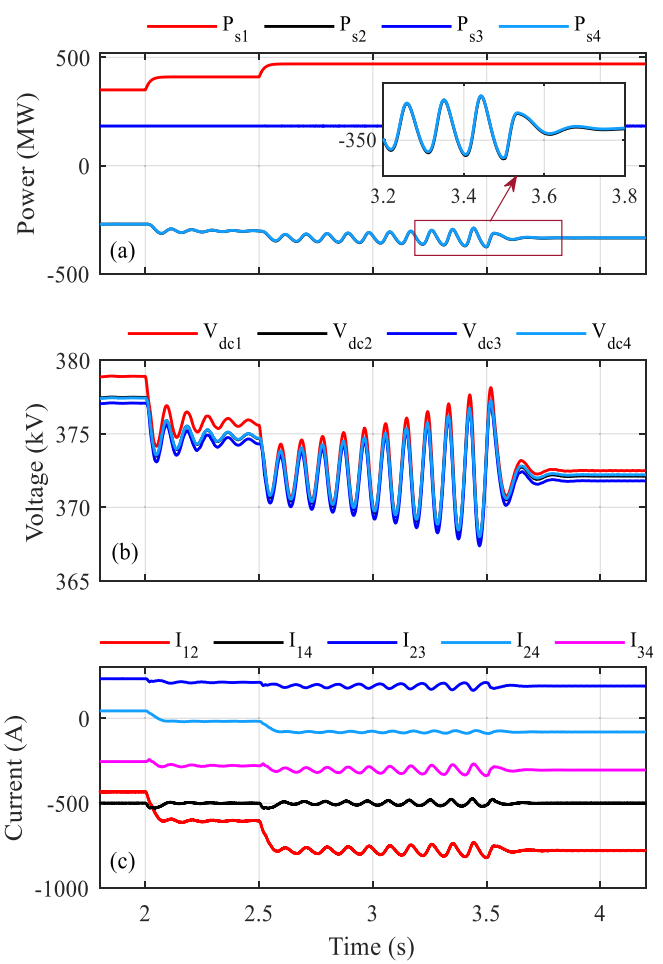

FIGURE 22. Impact of proposed LFO compensator on MTDC grid response.

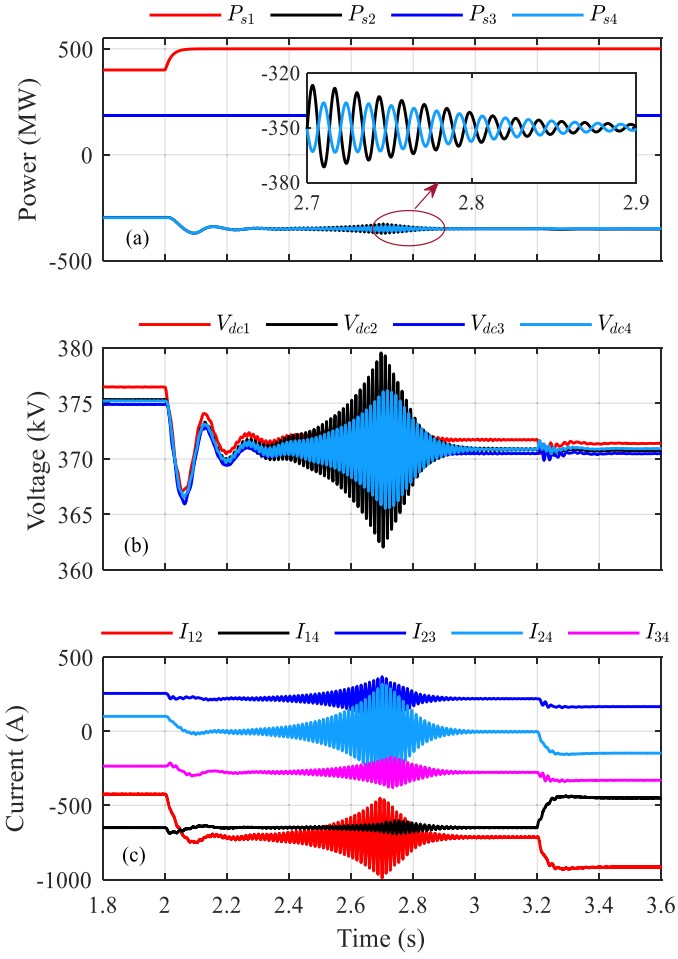

FIGURE 23. Impact of proposed MFO compensator on MTDC grid response.

environment, with the complete model parameters provided in the Appendix. MATLAB simulation results are cross-verified with real-time simulations conducted on the OPAL-RT Lab platform.

A. LFO COMPENSATOR PERFORMANCE

To verify the effectiveness of the LFO compensator, the MTDC grid is simulated with both droop voltage-controlled VSCs (VSC2 and VSC4) connected to a weak grid with an SCR = 1.4. Fig. 22 illustrates the system response to active power disturbances. Positive power values signify inverter operation, whereas negative values indicate rectifier operation. Initially, VSC1 and VSC3 inject 350 MW and 180 MW into the ac system, as shown in Fig. 22(a). The PFC regulates the line current I_{14} at -500 A. As the power injection of VSC1 increases to 410 MW at $t = 2$ s, the MTDC grid variables exhibit transient poorly damped oscillations, which are damped over time and do not compromise system stability. However, a further increase in P_{s1} to 470 MW at $t = 2.5$ s, induces unstable low-frequency oscillations at 10 Hz. These findings verify the eigenvalue analysis in Fig. 12(a), which predicts LFO instability at SCR = 1.4. The activation of the LFO compensator in both VSCs at $t = 3.5$ s mitigates these oscillations and stabilizes the system, demonstrating the high damping capability and effectiveness of the designed compensator. Fig. 22(c) confirms the ability of the PFC to maintain the line current I_{14} regulated at its reference value under the applied power disturbances.

B. MFO COMPENSATOR PERFORMANCE

In this study, the MTDC grid is simulated with both droop voltage-controlled VSCs interfaced to weak grids with an SCR = 1.15 to evaluate the performance of the MFO compensator as presented in Fig. 23. Initially, the system is in a stable state with both the LFO and MFO compensators activated, where the power injections of VSC1 and VSC3 are 400 MW and 180 MW, respectively. Concurrently, the PFC regulates the line current I_{14} at -650 A. At $t = 2$ s, there is a stepwise increase in P_{s1} to 500 MW, coinciding with the deactivation of the MFO compensator. The droop voltage controllers increase P_{s2} and P_{s4} to maintain the balance of power (Fig. 23(a)). This results in unstable medium-frequency oscillations at 72.8

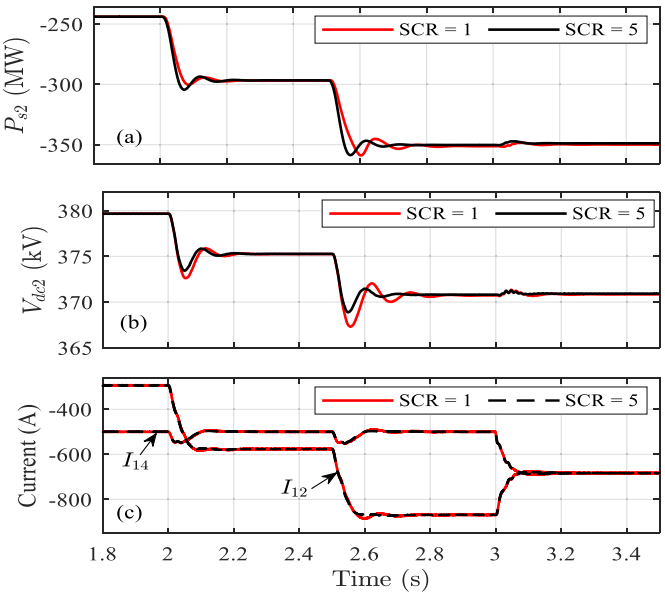

FIGURE 24. Performance of the proposed compensators against SCR variation. .

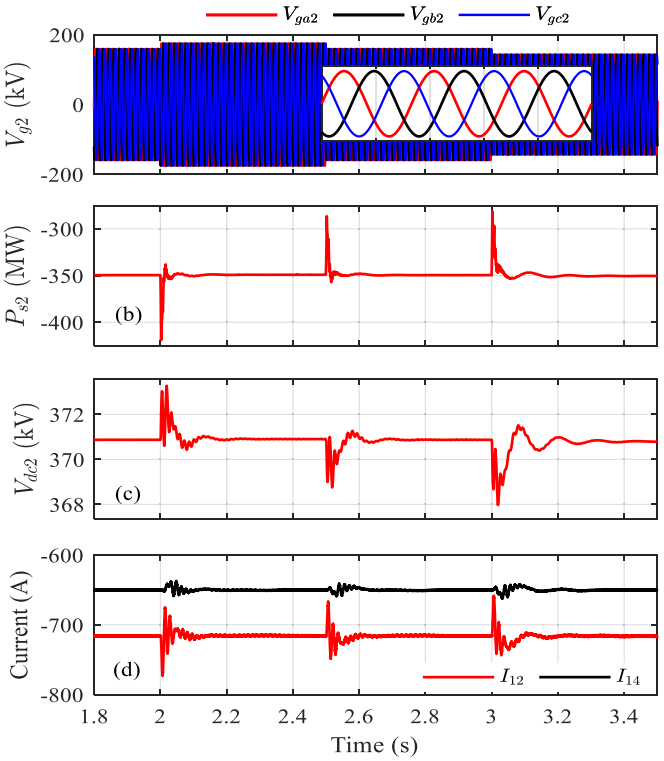

FIGURE 25. Performance of the proposed compensators against grid voltage disturbances.

Hz, which compromise the system stability, aligning with the eigenvalue analysis presented in Fig. 12(a). At $t = 2.7$ s, the MFO compensator is reactivated, which leads to the mitigation of the unstable oscillations and the stabilization of the system, verifying the efficacy of the designed MFO compensator. To assess the current tracking functionality of the PFC with the MFO compensator, I_{14}^{*} is step changed to -450 A at $t = 3.2$ s. As depicted in Fig. 23(c), the PFC successfully regulates the current I_{14} to its new reference value, demonstrating the minimal impact of the MFO compensator on the PFC current controller.

C. ROBUSTNESS AGAINST SCR VARIATION

This study compares the MTDC grid response with the proposed compensators under stiff and very weak grid conditions. While the above studies demonstrated the effectiveness of both the LFO and MFO compensators in maintaining system stability under very weak grid conditions, ensuring the compensators' robustness at strong grid scenarios is also essential. Fig. 24 illustrates the MTDC grid selected variables responses when VSC2 is connected to a strong system (SCR = 5) and a very weak system (SCR = 1). Under active power variations at $t = 2$ s and $t = 2.5$ s, the results demonstrate the system stability and robustness under both SCR conditions. However, as depicted in Fig. 24(b), the dc voltage overshoot and settling time are slightly lower under a stiff system due to the higher damping. At t = 3s, the PFC is tasked to equalize the line currents I_{12} and I_{14}. The response in Fig. 24(c) shows that the PFC can effectively equalize the line currents under both strong and weak system conditions. The results in Fig. 24 demonstrate the robustness of the proposed compensators under both SCR and active power variations.

D. ROBUSTNESS AGAINST GRID VOLTAGE DISTURBANCES

Grid operators often require grid-connected VSC stations to be able to ride through voltage disturbances, including voltage sags and swells, to maintain grid stability and reliability. For instance, European codes require that HVDC converter stations remain connected to the grid if the grid voltage changes within $\pm 10\%$ of its nominal value [49]. Fig. 25 illustrates the MTDC grid response to a sequence of grid voltage disturbances: a 10% voltage swell at $t = 2$ s, a return to normal voltage at $t = 2.5$ s, followed by a 10% voltage sag at $t = 3$ s, conducted with VSC2 interfaced to a very weak grid with an SCR = 1.15. Apart from transient oscillations at the beginning and end of the grid voltage disturbances, the system variables are properly damped and stable, demonstrating the capability of the MTDC grid to ride through the grid voltage swell and sag disturbances. Owing to the proposed compensators, the dc voltage remains stable without remarkable stress, with a maximum overshoot of just 3 kV, as evident in Fig. 25(c). Moreover, Fig. 25(d) demonstrates the ability of the PFC to maintain the line current I_{14} regulated at its reference value during the grid voltage disturbances.

E. PERFORMANCE UNDER FAULT CONDITION

Single phase-to-ground (SPG) faults are the most common type of faults in the power system, accounting for approximately 70–80% of all faults encountered in the power system [50]. Herein, the performance of the MTDC grid is evaluated

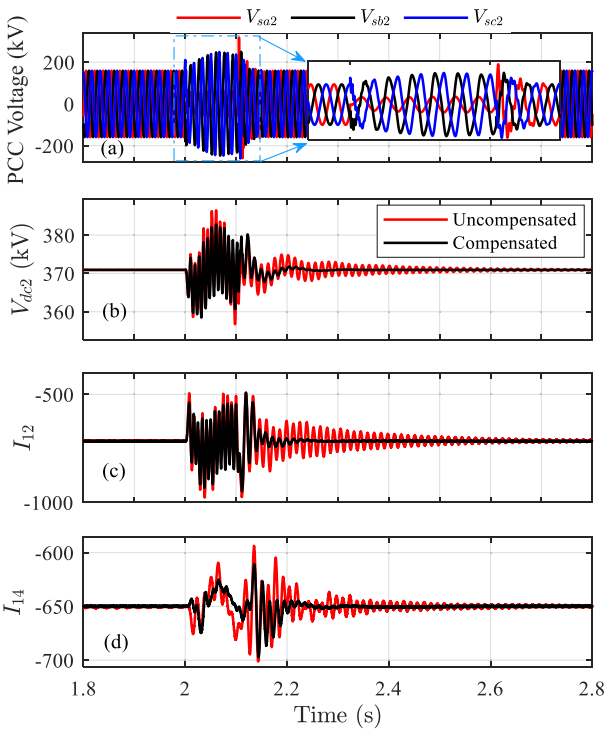

FIGURE 26. Performance of the proposed compensators under SPG fault.

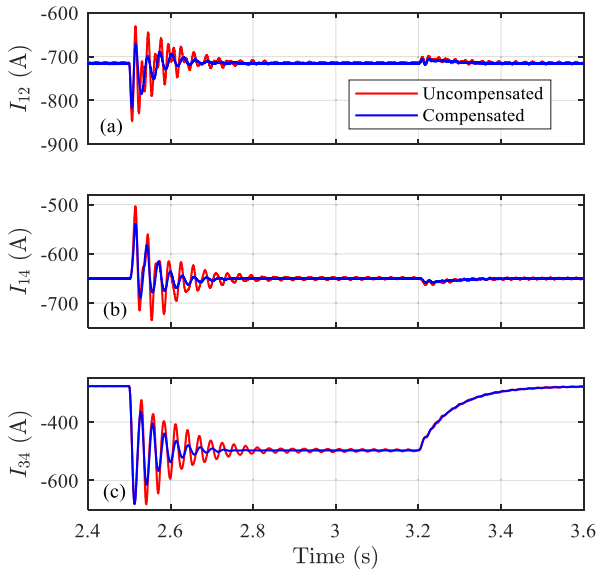

FIGURE 27. Performance of the proposed compensators under SPG fault.

under SPG faults with and without the proposed compensators, as illustrated in Fig. 26. At $t = 2$ s, as depicted in Fig. 26(a), an SPG fault occurs at the PCC of VSC2 for six cycles leading to a voltage sag of almost 62% in phase 'a' voltage. During the fault, the response of the selected MTDC grid variables reveals notable double-frequency oscillations in both the compensated and uncompensated models. However, the voltage and current overshoots are higher for the uncompensated model. After the fault clearance, at $t = 2.1$ s, the compensated system displays a significantly improved response with enhanced oscillation damping and much lower settling time compared to the uncompensated model. The settling time of the compensated response is 100 ms compared to 350 ms for the uncompensated model. The results of this study highlight the significant improvement of the MTDC grid dynamic performance under fault conditions when equipped with the proposed compensators. It is worth highlighting that no double-frequency oscillations are superimposed on the line current I_{14} response, as evident in Fig. 26(d), owing to the large grid inductance between VSC2 and line L14.

F. PERFORMANCE UNDER DC TRANSMISSION LINE OUTAGE

The tripping of dc transmission lines due to faults in an MTDC grid can severely disrupt its operation. To further investigate the performance of the proposed compensators under large system disturbances, Fig. 27 shows the selected current responses of the MTDC grid under the outage of the transmission line connecting VSC2 and VSC3 (L23). Following the disconnection of L23 at $t = 2.5$ s, the dc current of VSC3 is only routed through line L34, leading to a surge in current I_{34} as depicted in Fig. 27(c). The disconnection of L23 induces significant current oscillations due to the sudden variation in the system impedance. As shown in Fig. 27, the compensated system shows improved dynamic response, characterized by higher damping and reduced overshoot after the disturbance, compared to the uncompensated system. When L23 is reconnected at $t = 3.2$ s s, the current responses display no oscillations due to the gradual change in the system impedance.

G. REAL-TIME SIMULATION VALIDATION

Real-time (RT) simulation tests are carried out to assess the effectiveness of the proposed LFO and MFO compensators in real-time implementation. An RT simulation testbed using the OPAL-RT OP5600, equipped with a Virtex-6 FPGA, is used to simulate the power circuit of the MTDC grid, as depicted in Fig. 28. The proposed compensators are implemented in real-time, and the results are captured using a four-channel 500 MHz oscilloscope. The system parameters employed for RT tests are the same as those used in simulation studies, as provided in the Appendix. The RT simulation results of the performed test scenarios are depicted in Fig. 29 to 31.

The study shown in Fig. 26 assesses the RT performance of the LFO compensator by reapplying the test scenario presented in Fig. 21. As the active power increases, the system is subjected to a 10 Hz unstable LFO. Activating the LFO compensator damps the oscillations effectively, thereby restoring system stability. The RT results show close agreement with the simulation results in Fig. 21, confirming the feasibility of the LFO compensator in real-time implementation. The RT performance of the MFO compensator is demonstrated in Fig. 27.

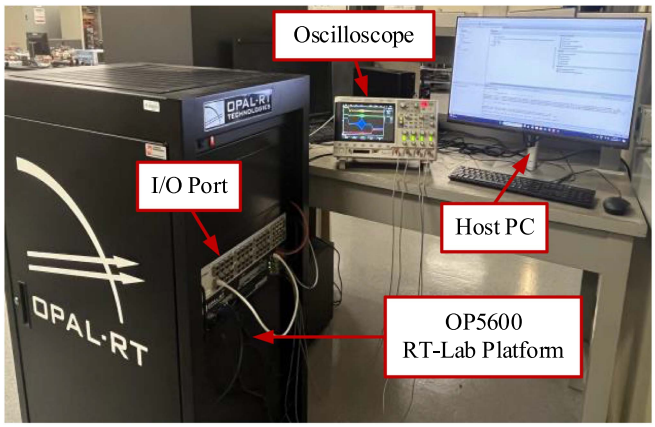

FIGURE 28. Real-time simulation testbed.

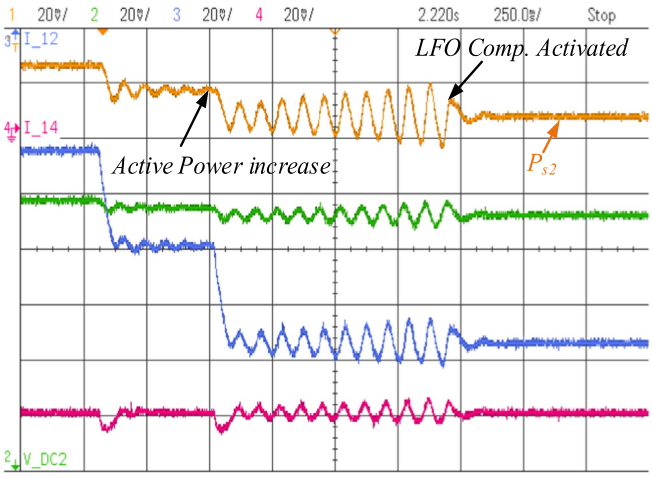

FIGURE 29. Real-time simulation validation of the LFO compensator effectivness.

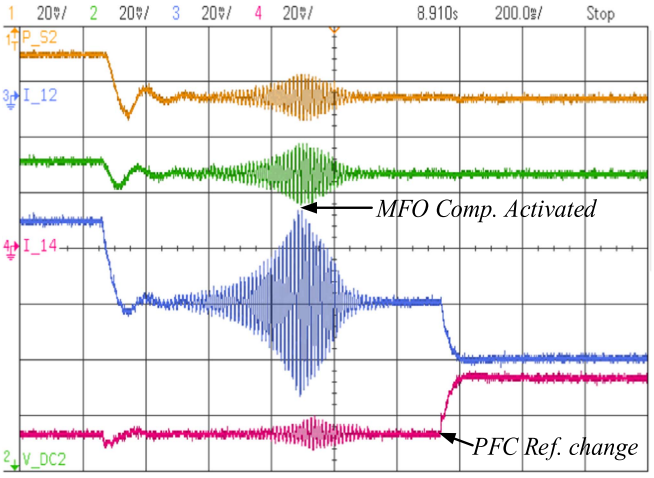

FIGURE 30. Real-time simulation validation of the MFO compensator effectiveness.

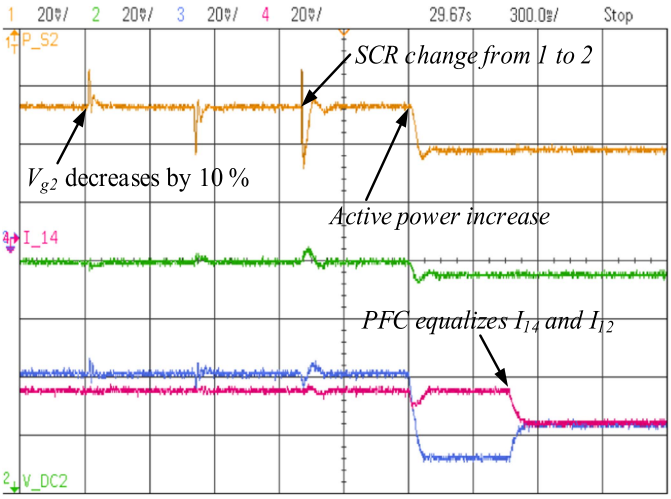

FIGURE 31. Real-time simulation performance of the proposed compensators under grid voltage disturbances.

The active power step up at $t = 2$ s results in unstable MFO at 72 Hz, compromising the system stability. The activation of the MFO compensator mitigated the unstable oscillations, aligning with the simulation results shown in Fig. 22.

The study shown in Fig. 28 evaluates the RT performance of both the LFO and MFO compensators under a series of grid side disturbances: a 10% grid voltage reduction at $t = 2$ s, a return to normal grid voltage $t = 2.5$ s and a significant SCR change from 1 to 2 at $t = 3$ s. The results highlight the ability of the system to maintain stability under various disturbances, verifying the robustness of the proposed compensators. At $t = 3.5$ s, VSC2 smoothly ramps up its rectification power in response to a 100 MW surge in power injection from VSC1. Finally, at $t = 4$ s, the PFC is commanded to equalize the line currents I_{14} and I_{12}. The PFC successfully equalizes the line currents, affirming the minimal impact of the MFO compensator on the PFC current tracking functionality.

VI. CONCLUSION

This paper addressed the stability and dynamic stabilization of a high-voltage VSC-based MTDC grid integrated with a PFC under extremely weak ac system conditions. The study reveals that system stability is particularly jeopardized when a droop voltage-controlled VSC is connected to a very weak system under rectifier operation, leading to both LFO and MFO compromising the system's stability. These oscillations become more prominent when multiple droop voltage-controlled VSCs are connected to very weak ac systems. In this scenario, unstable LFO and MFO were observed at SCR values of 1.4 and 1.8, respectively. The PFA revealed that the LFO is primarily attributed to the interactions between the PLL and the outer control loops of the VSC. In contrast, the MFO is mainly influenced by the dc-side states. Sensitivity analysis, using the derived linear state-space model, showed that PFC control parameters can significantly affect

the MTDC grid damping, and their fine-tuning is necessary to ensure adequate stability margin. Two effective compensators are proposed to address the identified LFO and MFO and enhance the system stability margins. Notably, the MFO compensator is integrated with the PFC controller, thereby expanding the PFC functionality to system stabilization in addition to power flow management. Extensive simulation studies verified the analytical analysis and the compensator efficacy. Moreover, real-time simulation tests are carried out to confirm the feasibility of the proposed compensators for real-time implementation.

APPENDIX

TABLE 2. MTDC GRID Parameters [51], [52]

Parameter	Value	Parameter	Value
Grid Parameters		VSC Control Parameters	
V_{L-L}	195 kV	$G_c(s)$	$(28.8s + 545)/s$
f	60 Hz	$G_{pll}(s)$	$(0.00093s + 0.02457)/s$
X/R	10	$G_P(s)$	$(1.21e^{-7}s + 2.11e^{-4})/s$
AC Filter		$G_{ac}(s)$	$(631849.32s)/s$
R_f	1.09 Ω	k_d	12e3 kW/V
L_f	57.6 mH	PFC Parameters	
C_f	4.15 µF	V_{PFC}	3 kV
MTDC grid		$G_{PFC}(s)$	$(0.0059s + 0.1268)/s$
V_{dc}	400 kV	Compensators parameters	
C_{dc}	150 µF	k_{LF}	65e5
R	0.0114 Ω/km	ω_{LF}	100 rad/s
L	0.9356 mH/km	k_{MF}	1.8
C	0.0123 µF/km	ω_1, ω_2	560 rad/s, 360 rad/s

REFERENCES

[1] S. D. Tavakoli, E. Sanchez-Sanchez, E. Prieto-Araujo, and O. Gomis-Bellmunt, "DC voltage droop control design for MMC-Based multiterminal HVDC grids," *IEEE Trans. Power Del.*, vol. 35, no. 5, pp. 2414–2424, Oct. 2020.

[2] N. Chaudhuri, B. Chaudhuri, R. Majumder, and A. Yazdani, *Multi-terminal Direct-Current Grids: Modeling, Analysis, and Control*. Hoboken, NJ, USA: Wiley, 2014.

[3] J. Blau, "Europe plans a North Sea grid," *IEEE Spectr.*, vol. 47, no. 3, pp. 12–13, Mar. 2010.

[4] K. Sun, H. Xiao, and Y. Liu, "Optimized allocation method of the VSC-MTDC system for frequency regulation reserves considering ancillary service cost," *CSEE J. Power Energy Syst.*, vol. 8, no. 1, pp. 53–63, Jan. 2022.

[5] L. Wang and M. S. Nguyen Thi, "Comparative stability analysis of offshore wind and marine-current farms feeding into a power grid using HVDC links and HVAC line," *IEEE Trans. Power Del.*, vol. 28, no. 4, pp. 2162–2171, Oct. 2013.

[6] J. Renedo, A. Garcia-Cerrada, and L. Rouco, "Active power control strategies for transient stability enhancement of AC/DC grids with VSC-HVDC multi-terminal systems," *IEEE Trans. Power Syst.*, vol. 31, no. 6, pp. 4595–4604, Nov. 2016.

[7] J. Renedo, A. Garcia-Cerrada, and L. Rouco, "Reactive-Power coordination in VSC-HVDC multi-terminal systems for transient stability improvement," *IEEE Trans. Power Syst.*, vol. 32, no. 5, pp. 3758–3767, Sep. 2017.

[8] Y. Liu, A. Raza, K. Rouzbehi, B. Li, D. Xu, and B. W. Williams, "Dynamic resonance analysis and oscillation damping of multiterminal DC grids," *IEEE Access*, vol. 5, pp. 16974–16984, 2017.

[9] G. Pinares and M. Bongiorno, "Methodology for the analysis of dc-network resonance-related instabilities in voltage-source converter-based multi-terminal HVDC systems," *IET Gener., Transmiss. Distrib.*, vol. 12, no. 1, pp. 170–177, 2018.

[10] F. Mura, C. Meyer, and R. W. De Doncker, "Stability analysis of high-power DC grids," *Conf. Rec. - Ind. Commer. Power Syst. Tech. Conf.*, vol. 46, no. 2, pp. 584–592, 2009.

[11] G. Pinares and M. Bongiorno, "Modeling and analysis of VSC-Based HVDC systems for DC network stability studies," *IEEE Trans. Power Del.*, vol. 31, no. 2, pp. 848–856, Apr. 2016, doi: 10.1109/TPWRD.2015.2455236.

[12] F. Thams, R. Eriksson, and M. Molinas, "Interaction of droop control structures and its inherent effect on the power transfer limits in multiterminal VSC-HVDC," *IEEE Trans. Power Del.*, vol. 32, no. 1, pp. 182–192, Feb. 2017.

[13] L. Guo, P. Li, X. Li, F. Gao, D. Huang, and C. Wang, "Reduced-order modeling and dynamic stability analysis of MTDC systems in DC voltage control timescale," *CSEE J. Power Energy Syst.*, vol. 6, no. 3, pp. 591–600, Sep. 2020.

[14] Q. Hao, Z. Li, F. Gao, and J. Zhang, "Reduced-order small-signal models of modular multilevel converter and MMC-based HVDC grid," *IEEE Trans. Ind. Electron.*, vol. 66, no. 3, pp. 2257–2268, Mar. 2019.

[15] Q. Fu, W. Du, H. Wang, X. Ma, and X. Xiao, "DC voltage oscillation stability analysis of DC-Voltage-Droop-Controlled multiterminal DC distribution system using Reduced-Order modal calculation," *IEEE Trans. Smart Grid*, vol. 13, no. 6, pp. 4327–4339, Nov. 2022.

[16] S. Sanchez, A. Garces, G. Bergna-Diaz, and E. Tedeschi, "Dynamics and stability of meshed multiterminal HVDC networks," *IEEE Trans. Power Syst.*, vol. 34, no. 3, pp. 1824–1833, May 2019.

[17] N. R. Chaudhuri, R. Majumder, B. Chaudhuri, and J. Pan, "Stability analysis of VSC MTDC grids connected to multimachine AC systems," *IEEE Trans. Power Del.*, vol. 26, no. 4, pp. 2774–2784, Oct. 2011.

[18] Q. Fu, W. Du, H. Wang, B. Ren, and X. Xiao, "Small-Signal stability analysis of a VSC-MTDC system for investigating DC voltage oscillation," *IEEE Trans. Power Syst.*, vol. 36, no. 6, pp. 5081–5091, Nov. 2021.

[19] M. Hassan, M. J. Hossain, and R. Shah, "Impact of meshed HVDC grid operation and control on the dynamics of AC/DC systems," *IEEE Syst. J.*, vol. 15, no. 4, pp. 5209–5220, Dec. 2021.

[20] Y. Liao, H. Wu, X. Wang, M. Ndreko, R. Dimitrovski, and W. Winter, "Stability and sensitivity analysis of Multi-Vendor, Multi-Terminal HVDC systems," *IEEE Open J. Power Electron.*, vol. 4, pp. 52–66, Jan. 2023.

[21] W. Zheng, J. Hu, and X. Yuan, "Modeling of vscs considering input and output active power dynamics for multi-Terminal HVDC interaction analysis in DC voltage control timescale," *IEEE Trans. Energy Convers.*, vol. 34, no. 4, pp. 2008–2018, Dec. 2019.

[22] D. Dong, B. Wen, D. Boroyevich, P. Mattavelli, and Y. Xue, "Analysis of phase-locked loop low-frequency stability in three-phase grid-connected power converters considering impedance interactions," *IEEE Trans. Ind. Electron.*, vol. 62, no. 1, pp. 310–321, Jan. 2015.

[23] X. He and H. Geng, "PLL synchronization stability of grid-connected multiconverter systems," *IEEE Trans. Ind. Appl.*, vol. 58, no. 1, pp. 830–842, Jan./Feb. 2022.

[24] M. F. M. Arani and Y. A. R. I. Mohamed, "Analysis and performance enhancement of vector-controlled VSC in HVDC links connected to very weak grids," *IEEE Trans. Power Syst.*, vol. 32, no. 1, pp. 684–693, Jan. 2017.

[25] X. Lin, J. Yu, R. Yu, J. Zhang, Z. Yan, and H. Wen, "Improving small-signal stability of grid-connected inverter under weak grid by decoupling phase-lock loop and grid impedance," *IEEE Trans. Ind. Electron.*, vol. 69, no. 7, pp. 7040–7053, Jul. 2022.

[26] H. Wu and X. Wang, "Design-oriented transient stability analysis of grid-connected converters with power synchronization control," *IEEE Trans. Ind. Electron.*, vol. 66, no. 8, pp. 6473–6482, Aug. 2019.

[27] A. Asrari, M. Mustafa, M. Ansari, and J. Khazaei, "Impedance analysis of virtual synchronous generator-based vector controlled converters for weak AC grid integration," *IEEE Trans. Sustain. Energy*, vol. 10, no. 3, pp. 1481–1490, Jul. 2019.

[28] C. Guo, W. Liu, C. Zhao, and R. Iravani, "A Frequency-Based synchronization approach for the VSC-HVDC station connected to a weak AC grid," *IEEE Trans. Power Del.*, vol. 32, no. 3, pp. 1460–1470, Jun. 2017.

[29] C. Li, W. Liu, J. Liang, X. Ding, and L. M. Cipcigan, "Improved grid impedance compensation for phase-locked loop to stabilize the very-weak-grid connection of VSIs," *IEEE Trans. Power Del.*, vol. 37, no. 5, pp. 3863–3872, Oct. 2022.
[30] S. Lu, Z. Xu, L. Xiao, W. Jiang, and X. Bie, "Evaluation and enhancement of control strategies for VSC stations under weak grid strengths," *IEEE Trans. Power Syst.*, vol. 33, no. 2, pp. 1836–1847, Mar. 2018.
[31] Z. Xie, Y. Chen, W. Wu, W. Gong, and J. M. Guerrero, "Stability enhancing voltage feedforward inverter control method to reduce the effects of phase-locked loop and grid impedance," *IEEE J. Emerg. Sel. Top. Power Electron.*, vol. 9, no. 3, pp. 3000–3009, Jun. 2021.
[32] S. Silwal, M. Karimi-Ghartemani, H. Karimi, M. Davari, and S. M. H. Zadeh, "A multivariable controller in synchronous frame integrating phase-locked loop to enhance performance of Three-Phase Grid-Connected inverters in weak grids," *IEEE Trans. Power Electron.*, vol. 37, no. 9, pp. 10348–10359, Sep. 2022.
[33] C. Li, S. Wang, F. Colas, and J. Liang, "Dominant instability mechanism of VSI connecting to a very weak grid," *IEEE Trans. Power Syst.*, vol. 37, no. 1, pp. 828–831, Jan. 2022.
[34] L. Dewangan and H. J. Bahirat, "Robust decoupled Outer-Control design for single VSC and HVDC grid with controller weak AC system interconnection," *IEEE Trans. Power Del.*, vol. 37, no. 3, pp. 2337–2347, Jun. 2022.
[35] L. Dewangan and H. J. Bahirat, "Controller interaction and stability margins in mixed SCR MMC-Based HVDC grid," *IEEE Trans. Power Syst.*, vol. 35, no. 4, pp. 2835–2846, Jul. 2020.
[36] Y. Wang, C. Zhao, and R. Iravani, "Small signal stability investigation of the MMC-HVDC grid," *IEEE Trans. Power Del.*, vol. 37, no. 5, pp. 4448–4459, Oct. 2022.
[37] L. Liu, Z. Liu, M. Popov, P. Palensky, and M. A. M. M. Van Der Meijden, "A fast protection of multi-terminal HVDC system based on transient signal detection," *IEEE Trans. Power Del.*, vol. 36, no. 1, pp. 43–51, Feb. 2021.
[38] S. Zhang, G. Zou, X. Wei, and C. Sun, "Diode-Bridge multiport hybrid DC circuit breaker for multiterminal DC grids," *IEEE Trans. Ind. Electron.*, vol. 68, no. 1, pp. 270–281, Jan. 2021.
[39] H. R. A. Mohamed and Y. A. R. I. Mohamed, "Assessment and mitigation of DC breaker impacts on VSC-MTDC grid equipped with power flow controller," *IEEE Open J. Power Electron.*, vol. 4, pp. 237–251, Feb. 2023.
[40] W. Wang, M. Barnes, O. Marjanovic, and O. Cwikowski, "Impact of DC breaker systems on multiterminal VSC-HVDC stability," *IEEE Trans. Power Del.*, vol. 31, no. 2, pp. 769–779, Apr. 2016.
[41] M. Abbasipour and X. Liang, "Power flow study of MT-HVDC grid compensated by multiport interline DC power flow controller," *IEEE Trans. Ind. Appl.*, vol. 59, no. 4, pp. 4786–4796, Jul./Aug. 2023.
[42] J. Sau-Bassols, E. Prieto-Araujo, O. Gomis-Bellmunt, and F. Hassan, "Series interline DC/DC current flow controller for meshed HVDC grids," *IEEE Trans. Power Del.*, vol. 33, no. 2, pp. 881–891, Apr. 2018.
[43] D. Jovcic and B. T. Ooi, "Developing DC transmission networks using DC transformers," *IEEE Trans. Power Del.*, vol. 25, no. 4, pp. 2535–2543, Oct. 2010.
[44] C. D. Barker and R. S. Whitehouse, "A current flow controller for use in HVDC grids," in *Proc. 10th IET Int. Conf. AC DC Power Transmiss.*, 2012, pp. 1–15.
[45] W. Wu, X. Wu, Y. Zhao, and L. Jing, "Active damping control of Multiport DC power follow controller for suppressing Sub-Synchronous oscillation," *Dianwang Jishu/Power Syst. Technol.*, vol. 45, no. 4, pp. 1388–1399, 2021.
[46] H. R. A. Mohamed and Y. A. R. I. Mohamed, "Active damping of VSC-MTDC grid equipped with interline power flow controller," *IEEE Access*, vol. 10, pp. 54372–54385, 2022.
[47] H. R. A. Mohamed and Y. A. R. I. Mohamed, "Comprehensive analysis and stabilization of a B2B HVDC system connecting two extremely weak grids considering the impact of power feedforward compensation," *IEEE Open J. Power Electron.*, vol. 5, pp. 336–351, 2024.
[48] W. Wu, X. Wu, Y. Zhao, L. Wang, T. Zhao, and L. Jing, "An improved multiport DC power flow controller for VSC-MTDC grids," *IEEE Access*, vol. 8, pp. 7573–7586, 2020.
[49] "COMMISSION REGULATION (EU) 2016/1447 of 26 August 2016. Establishing a network code on requirements for grid connection of high voltage direct current systems and direct current-connected power park modules," *Off. J. Eur. Union*, vol. 59, no. L 241, pp. 1–65, 2016.
[50] X. Wang, J. Gao, X. Wei, Z. Zeng, Y. Wei, and M. Kheshti, "Single line to ground fault detection in a non-effectively grounded distribution network," *IEEE Trans. Power Del.*, vol. 33, no. 6, pp. 3173–3186, Dec. 2018.
[51] E. Prieto-Araujo, A. Egea-Alvarez, S. F. Fekriasl, and O. Gomis-Bellmunt, "DC voltage droop control design for multiterminal HVDC systems considering AC and DC grid dynamics," *IEEE Trans. Power Del.*, vol. 31, no. 2, pp. 575–585, Apr. 2016.
[52] K. Rouzbehi, A. Miranian, J. I. Candela, A. Luna, and P. Rodriguez, "A generalized voltage droop strategy for control of multiterminal DC grids," *IEEE Trans. Ind. Appl.*, vol. 51, no. 1, pp. 607–618, Jan./Feb. 2015.

HASSANIEN RAMADAN A. MOHAMED (Graduate Student Member, IEEE) was born in Qena, Egypt, in 1992. He received the B.Sc. degree from the Faculty of Engineering, South Valley University, Qena, Egypt, in 2013, and the M.Sc. degree from the Budapest University of Technology and Economics, Budapest, Hungary, in 2018. He is currently working toward the Ph.D. degree with the Department of Electrical and Computer Engineering, University of Alberta, Edmonton, AB, Canada. His research interests include dynamics and control of power electronic converters for MTDC grids and optimal grid integration of renewable energy resources and electric vehicles.

YASSER ABDEL-RADY I. MOHAMED (Fellow, IEEE) was born in Cairo, Egypt, in 1977. He received the B.Sc. (Hons.) and M.Sc. degrees in electrical engineering from Ain Shams University, Cairo, Egypt, in 2000 and 2004, respectively, and the Ph.D. degree in electrical engineering from the University of Waterloo, Waterloo, ON, Canada, in 2008. He is currently a Professor with the Department of Electrical and Computer Engineering, University of Alberta, Edmonton, AB, Canada. His highly cited research interests include modeling, analysis, stability, control, and optimization of power electronic converters and systems, active distribution systems, and microgrids; grid integration of distributed and renewable energy resources and energy storage; and the development of artificial intelligence technologies for smart grids. Dr. Mohamed is an Associate Editor for IEEE TRANSACTIONS ON POWER ELECTRONICS. He was the Editor of IEEE TRANSACTIONS ON POWER SYSTEMS, IEEE TRANSACTIONS ON SMART GRID, and IEEE POWER ENGINEERING LETTERS, and an Associate Editor for IEEE TRANSACTIONS ON INDUSTRIAL ELECTRONICS. Dr. Mohammed is an Elected Fellow of the Asia-Pacific Artificial Intelligence Association. He is a registered Professional Engineer in the Province of Alberta, Canada.

EHAB FAHMY EL-SAADANY (Fellow, IEEE) was born in Cairo, Egypt, in 1964. He received the B.Sc. and M.Sc. degrees in electrical engineering from Ain Shams University, Cairo, Egypt, in 1986 and 1990, respectively, and the Ph.D. degree in electrical engineering from the University of Waterloo, Waterloo, ON, Canada, in 1998. He was a Professor with the Electrical and Computer Engineering Department, University of Waterloo, till 2019, where he was also the Director of the Power M.Eng. program between 2010 and 2015. He is also a Professor with the Department of Electrical Engineering and the Dean of the College of Engineering and Physical Sciences, Khalifa University, Abu Dhabi, UAE. He is an internationally recognized expert in the area of sustainable energy integration and smart distribution systems. His research interests include smart grid operation and control, microgrids, transportation electrification, self-healing, cyber-physical security of smart grids, protection, power quality, and embedded generation. He is a Registered Professional Engineer in the Province of Ontario. He is currently an IEEE Fellow for his contributions to distributed generation planning, operation, and control.